

Exploring a lower resolution physics grid in CAM-SE-CSLAM

Adam R. Herrington^{1*}, Peter H. Lauritzen², Kevin A. Reed¹, Steve Goldhaber², Brian E. Eaton²

¹School of Marine and Atmospheric Sciences, Stony Brook University, Stony Brook, New York

²National Center for Atmospheric Research, Boulder, Colorado, USA

Key Points:

- Control volumes are defined to provide an isotropic representation of the numerics to the physics.
- Grid imprinting from the spectral-element method is eliminated in regions with steep terrain, using the coarser physics grid.
- The coarser physics grid does not degrade the effective resolution of the model.

*Stony Brook, New York

Corresponding author: Adam R. Herrington, adam.herrington@stonybrook.edu

12 **Abstract**

13 This paper describes the implementation of a coarser resolution physics grid into the Com-
 14 munity Atmosphere Model (CAM). The dry dynamics is represented by the spectral el-
 15 ement dynamical core and tracer transport is computed using the Conservative Semi-
 16 Lagrangian Finite Volume Method (CAM-SE-CSLAM). Algorithms are presented that
 17 map fields between the dynamics and physics grids while maintaining numerical proper-
 18 ties ideal for atmospheric simulations such as mass conservation and mixing ratio shape
 19 and linear-correlation preservation. The results of experiments using the lower resolution
 20 physics grid are compared to the conventional method in which the physics and dynami-
 21 cal grids coincide. The lower resolution physics grid consists of control volumes designed
 22 to provide an isotropic representation of the dynamics to the physical parameterizations,
 23 and eliminates grid imprinting, even in regions with steep topography. The impact of the
 24 coarser resolution physics grid on the resolved scales of motion is analyzed in an aqua-
 25 planet configuration, across a range of dynamical core grid resolutions. The results sug-
 26 gest that the effective resolution of the model is not degraded through the use of a coarser
 27 resolution physics grid. Since the physics makes up about half the computational cost of
 28 the conventional CAM-SE-CSLAM configuration, the coarser physics grid may allow for
 29 significant cost savings with little to no downside.

30 **1 Introduction**

31 Global atmospheric models fundamentally consist of two components. The dynam-
 32 ical core (*dynamics*), which numerically integrate the adiabatic equations of motion and
 33 tracer advection, and the physical parameterizations (*physics*), which compute the effects
 34 of diabatic and subgrid-scale processes (e.g., radiative transfer and moist convection) on
 35 the grid-scale. More out of convenience than anything else, the physics are evaluated on
 36 the dynamics grid, i.e., the physics and dynamics grids coincide. From linear stability and
 37 accuracy analysis of numerical methods, it is a common result that the shortest simulated
 38 wavelengths are not accurately represented by the dynamical core. Additionally, simulated
 39 downscale cascades result in an unrealistic collection of energy and/or enstrophy near the
 40 truncation scale, which may be observed from kinetic energy spectra in model simulations
 41 [Skamarock, 2011]. Some form of dissipation must be incorporated into models to miti-
 42 gate these numerical artifacts near the grid scale [Jablonowski and Williamson, 2011]. The
 43 unrealistic nature of the grid-scale led Lander and Hoskins [1997] to speculate whether the

44 physics should be evaluated on a grid that is more reflective of the scales actually resolved
 45 by the dynamical core.

46 Exploring the impact of different physics grid resolutions has so far been limited to
 47 models employing the spectral transform method [*Lander and Hoskins*, 1997; *Williamson*,
 48 1999; *Wedi*, 2014]. *Lander and Hoskins* [1997] argued that passing under-resolved states
 49 to the physics may be especially problematic in spectral transform models, since the physics
 50 are evaluated on a latitude-longitude transform grid, and contains more degrees of free-
 51 dom than the spectral representation to prevent aliasing of quadratic quantities. However,
 52 *Lander and Hoskins* [1997] found that the spectral truncation of the physics tendencies
 53 damps errors that may result from passing an under-resolved state to the physics, although
 54 the extent to which these errors may still be present in the model is difficult to address.

55 Another class of spectral transform models evaluate the quadratic terms using semi-
 56 Lagrangian methods, which are implicitly diffusive, relaxing constraints on the resolution
 57 of the transform grid. *Wedi* [2014] experimented with different transform grid resolutions
 58 and concluded that the standard high resolution quadratic grid actually improves fore-
 59 cast skill over the use of a lower-resolution transform grid. They suggest that increasing
 60 the resolution of the transform grid simulates a kind of sub-grid variability on the spec-
 61 tral state, which is thought to be under-represented in global atmospheric models [*Shutts*,
 62 2005]. This is in principle the purpose of "super-parameterization," in which a cloud re-
 63 solving model is embedded in each grid cell to approximate sub-grid variability, and im-
 64 proves both diurnal and sub-seasonal variability in the model [*Randall et al.*, 2003].

65 After the physics tendencies are transformed into spectral space, it is possible to
 66 truncate the tendencies at any particular wave number in global spectral transform models.
 67 *Williamson* [1999] conducted a pair of convergence tests using a spectral transform model;
 68 a conventional convergence test and one in which the spectral truncation of the physics
 69 tendencies is held fixed and the resolution of the dynamical core increased. In contrast to
 70 the realistic weather forecasts of *Wedi* [2014], *Williamson* [1999] ran their model to equi-
 71 librium in an idealized climate configuration. When the physics and dynamics resolutions
 72 increase together, as in more typical convergence studies, the strength of the Hadley Cell
 73 increases monotonically with resolution. This sensitivity of Hadley Cell strength to hori-
 74 zontal resolution is a common result of global models at hydrostatic resolutions [see *Her-*
rington and Reed, 2017, and references therein]. But with the truncation wave number of

physics tendencies held fixed, the Hadley Cell showed very little sensitivity to dynamical core resolution, resembling the solution for which the dynamics truncation wave number is equal to that of the lower resolution physics. *Herrington and Reed* [2017] speculated that these results suggest the scales of motion resolved by the dynamical core may be aliased to the lower resolution physics.

Global spectral transform models, while remarkably efficient at small processor counts, do not scale well on massively parallel systems. High-order Galerkin methods are becoming increasingly popular in climate and weather applications due to their high-parallel efficiency, high-processor efficiency, high-order accuracy (for smooth problems), and geometric flexibility facilitating mesh-refinement applications [e.g., *Giraldo and Restelli*, 2008; *Nair et al.*, 2009; *Brdar et al.*, 2013, and the Energy Exascale Earth System Model; <https://e3sm.org/>]. High resolution climate simulations with NCAR's Community Atmosphere Model [CAM; *Neale et al.*, 2012] are typically performed using a continuous Galerkin dynamical core referred to as CAM-SE [CAM Spectral Elements; *Taylor et al.*, 2008; *Dennis et al.*, 2012; *Lauritzen et al.*, 2018]. CAM-SE may be optionally coupled to a conservative, semi-Lagrangian tracer advection scheme for accelerated multi-tracer transport [CAM-SE-CSLAM; *Lauritzen et al.*, 2017]. Tracer advection then evolves on an entirely separate, finite-volume grid which contains the same degrees of freedom as CAM-SE's quadrature node grid.

Element-based Galerkin methods are susceptible to grid-imprinting, and may need be considered when contemplating a particular physics grid [*Herrington et al.*, 2018, hereafter referred to as H18]. Grid imprinting manifests at the element boundaries, since the global basis is least smooth (C^0 ; all derivatives are discontinuous) for quadrature nodes lying on the element boundaries, and the gradients (e.g., pressure gradients) are systematically tighter producing local extremes. Through computing the physics tendencies at the nodal points, element boundary extrema is also observed in the physics tendencies.

H18 has shown that through evaluating the physics on the finite-volume tracer advection grid in CAM-SE-CSLAM, element boundary errors are substantially reduced, although still problematic in regions of steep terrain, at low latitudes. Through integrating CAM-SE's basis functions over the control volumes of the finite-volume grid, element boundary extrema is additionally weighted by the C^∞ solutions (i.e., the basis representation is infinitely smooth and all derivatives are continuous) that characterize the interior

108 of the element, and the state is smoother. Additionally, in defining an area averaged state,
109 the finite-volume physics grid is made consistent with assumptions inherent to the physics,
110 and is more appropriate for coupling to other model components (e.g., the land model),
111 which is typically performed using finite-volume based mapping algorithms.

112 The CAM-SE-CSLAM finite-volume grid is defined through dividing the elements
113 of CAM-SE's gnomonic cubed-sphere grid with equally spaced, equi-angular coordinate
114 lines parallel to the equi-angular element boundaries, such that there are 3×3 control
115 volumes per element (hereafter referred to as $pg3$; see Figure 1). While the physics grid
116 in H18 is $pg3$, i.e., the physics and dynamics grids have the same degrees of freedom, the
117 control volumes in $pg3$ encompass a region of the element in which their proximity to the
118 element boundaries are not equal. Therefore, not every control volume in an element has
119 the same smoothness properties. This may be avoided through defining a physics grid in
120 which the elements are instead divided into 2×2 control volumes (hereafter referred to as
121 $pg2$; see Figure 1). The control volumes of the $pg2$ grid all have the same proximity to
122 the element boundaries, and should mitigate the element boundary noise that remains in
123 the $pg3$ grid, and shown in H18.

124 In this study, we test the hypothesis that the coarser, $pg2$ physics grid is effective at
125 reducing spurious noise at element boundaries, particularly over regions of rough topogra-
126 phy. In addition, the recent trend towards running models at ever higher resolutions is an
127 almost prohibitive computational burden. As the physics are responsible for over half of
128 the computational cost in CAM-SE [Lauritzen *et al.*, 2018], the improvement in computa-
129 tional performance using a coarser resolution physics grid is potentially significant. How-
130 ever, any advantages of using a coarser physics grid need be weighed against any potential
131 reduction in simulation quality, e.g., possible aliasing of the resolved scales of motion by
132 the coarser grid, as suggested by the results of Williamson [1999]. Section 2 describes the
133 implementation of the $pg2$ grid into CAM-SE-CSLAM, and the idealized model configu-
134 rations used throughout this study. Section 3 provides results of model simulations, to test
135 the implementation of the mapping algorithms and identify any changes in grid imprint-
136 ing, and in the resolved scales of motion, compared with the $pg3$ configuration. Section 4
137 provides a discussion of the results and conclusions.

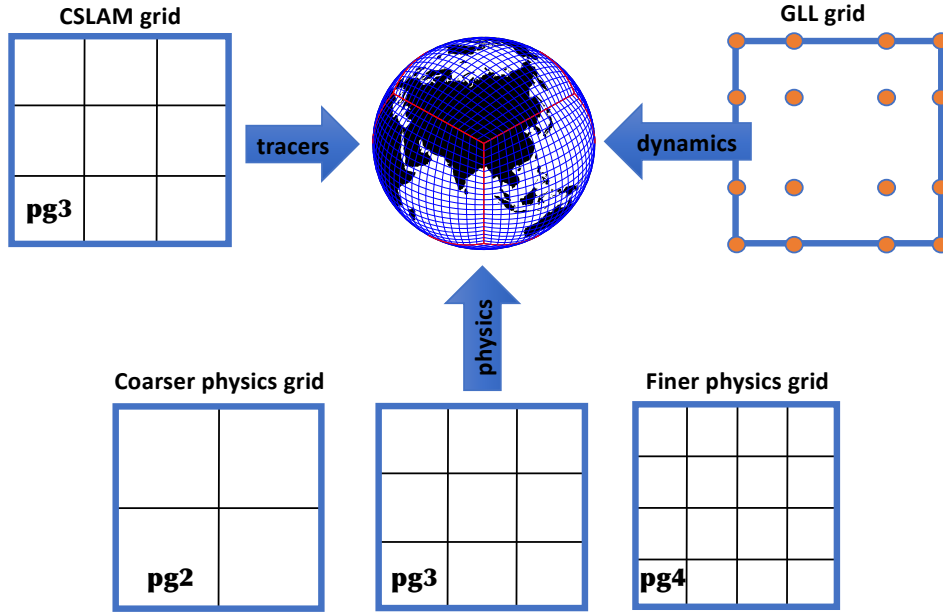


Figure 1. An overview of the different grids in CAM-SE-CSLAM.

155

2 Methods

138
139
140
141
142
143
144
145
146
147
148
149
150
151
152
153
154

Separating dynamics, tracer and physics grids introduces the added complexity of having to map the state from dynamics and tracer grids to the physics grid; and mapping physics tracer increments back to the tracer grid and physics increments needed by the dynamical core to the dynamics grid (see Figure 1). The dynamics grid in the case of CAM-SE-CSLAM refers to the Gauss-Lobatto-Legendre (GLL) quadrature nodes used by the spectral-element method to solve the momentum equations for the momentum vector (u, v), thermodynamics equation for temperature (T), continuity equation for dry air mass ($\frac{1}{g} p$), and continuity equations for water vapor and thermodynamically and inertially active condensates [see, e.g., *Lauritzen et al.*, 2018, for details]. By tracer grid we refer to the $pg3$ grid on which CSLAM performs tracer transport of water vapor, condensates and other tracers. Although water vapor and condensates are being advected by the CSLAM scheme on the $pg3$ grid, these quantities are also needed on the GLL grid for the momentum equations and thermodynamic equation. Transport of water variables is also performed by the spectral-element method on the GLL grid. To avoid decoupling of water species on the CSLAM and GLL grids, the GLL water species are overwritten by the CSLAM values every physics time-step. This is explained in detail in H18.

156 Similarly to the CAM-SE-CSLAM *pg3* configuration, the dynamics state (momentum vector, temperature, dry pressure) must be mapped from the *GLL* grid to the physics
 157 grid. Exactly the same algorithms as used in the *pg3* configuration apply, i.e. momentum
 158 components are interpolated by evaluating the internal Lagrange basis functions (used
 159 in the spectral-element method) at the equi-angular (gnomonic) center of the *pg2* cells
 160 and the Lagrange basis function representations of temperature and pressure are integrated
 161 over the *pg2* control volumes. See H18 for details.
 162

163 As compared to the *pg3* configuration, the extra complication with the *pg2* setup is
 164 that the tracer grid does not coincide with the physics grid, i.e. the tracer state needs to
 165 be mapped from the CSLAM grid (*pg3*) to the physics grid (*pg2*), and tracer increments
 166 computed by physics must be mapped from the physics grid back to the CSLAM grid. In
 167 order to describe the mapping algorithms between the grids some notation needs to be
 168 introduced.

169 The mapping algorithms are applied to each element Ω (with spherical area $\Delta\Omega$) so
 170 without loss of generality consider one element. Let $\Delta A_k^{(pg2)}$ and $\Delta A_\ell^{(pg3)}$ be the spherical
 171 area of the physics grid cell $A_k^{(pg2)}$ and CSLAM control volume $A_\ell^{(pg3)}$, respectively. The
 172 physics grid cells and CSLAM cells, respectively, span the element, Ω , without gaps or
 173 overlaps

$$\bigcup_{k=1}^{nphys^2} A_k^{(pg2)} = \Omega \text{ and } A_k^{(pg2)} \cap A_\ell^{(pg2)} = \emptyset \quad \forall k \neq \ell, \quad (1)$$

$$\bigcup_{k=1}^{nc^2} A_k^{(pg3)} = \Omega \text{ and } A_k^{(pg3)} \cap A_\ell^{(pg3)} = \emptyset \quad \forall k \neq \ell, \quad (2)$$

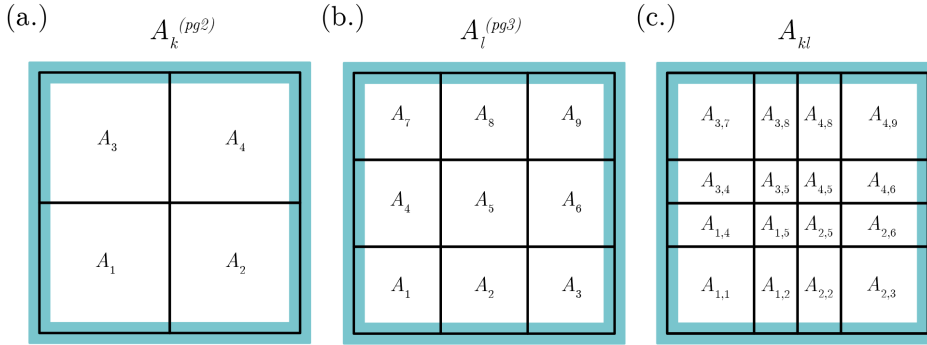
174 where $nc = 3$ is the CSLAM grid resolution parameter and $nphys = 2$ is the physics grid
 175 resolution parameter (following the Fortran code base), although the methods described
 176 here are valid for any arbitrary integer $nphys$ (e.g., $nphys = 4$ is shown in Figure 1). The
 177 overlap areas between the k -th physics grid cell and ℓ th CSLAM cell are denoted

$$A_{k\ell} = A_k^{(pg2)} \cap A_\ell^{(pg3)}, \quad (3)$$

178 (see Figure 2) so that

$$A_k^{(pg2)} = \bigcup_{\ell=1}^{nc^2} A_{k\ell}. \quad (4)$$

179 This overlap grid is also referred to as the *exchange grid*.



189

Figure 2. Indices notation for (a) the $pg2$ grid, (b) the $pg3$ grid and (c) their exchange grid.

180

2.1 Mapping tracers from $A^{(pg3)}$ to $A^{(pg2)}$ (CSLAM to physics grid)

181

The CSLAM and physics grids are both finite-volume grids so existing CSLAM technology can be used to map the tracer state from CSLAM to physics grid. That is, compute a high-order shape-preserving reconstruction of mixing ratio m and dry air mass $\frac{1}{g}\Delta p$ per unit area in each CSLAM control volume and integrate those reconstruction functions over the overlap areas [Lauritzen *et al.*, 2010; Nair and Lauritzen, 2010]. This algorithm retains the properties of CSLAM: inherent mass-conservation, consistency (constant mixing ratio is preserved), mixing ratio shape-preservation and linear-correlation preservation.

190

Denote the known cell averaged values of dry pressure-level thickness and mixing ratio $\overline{\Delta p}^{(pg3)}$ and $\overline{m}^{(pg3)}$, respectively. We consider a particular layer and for simplicity drop the layer subscript. The same procedure is applied to each layer in a column. The unknowns we would like to compute are the cell-averaged values of the same quantities on the physics grid; $\overline{\Delta p}^{(pg2)}$ and $\overline{m}^{(pg2)}$, respectively. The dry pressure level thickness integrated over the k 'th physics grid cell is given by

$$\overline{\Delta p}_k^{(pg2)} = \frac{1}{\Delta A_k^{(pg2)}} \sum_{\ell=1}^{nc^2} \langle \delta p \rangle_{k\ell}, \quad (5)$$

196

where $\langle \delta p \rangle_{k\ell}$ is the dry mass in a layer over overlap area $A_{k\ell}$. It is computed by integrating a high-order (2D polynomial of degree 2) reconstruction of pressure-level thickness in

198 each CSLAM cell over the overlap area $A_{k\ell}$

$$\langle \delta p \rangle_{k\ell} = \int_{A_{k\ell}} \left[\sum_{i+j \leq 2} \mathcal{P}_{\ell}^{(ij)} x^i y^j \right] dA. \quad (6)$$

199 The reconstruction coefficients $\mathcal{P}_{\ell}^{(ij)}$ in CSLAM cell ℓ are computed from the cell aver-
 200 age pressure level thicknesses on the CSLAM grid $\overline{\Delta p}^{(pg3)}$ and the numerical integration
 201 over overlap areas is done by line-integrals. The details of that are given in *Lauritzen et al.*
 202 [2010] and not repeated here.

203 The average tracer mass per unit area on the physics grid is given by

$$\overline{m\Delta p}_k^{(pg2)} = \frac{1}{\Delta A_k^{(pg2)}} \sum_{\ell=1}^{nc^2} \langle m\delta p \rangle_{k\ell}, \quad (7)$$

204 where $\langle m\delta p \rangle_{k\ell}$ is the tracer mass over $A_{k\ell}$ resulting from integrating a high-order recon-
 205 struction of Δp and m combined using the approach outlined in Appendix B of *Nair and*
 206 *Lauritzen* [2010] over the overlap area $A_{k\ell}$

$$\langle m\delta p \rangle_{k\ell} = \int_{A_{k\ell}} \left[\overline{\Delta p}_{\ell}^{(pg3)} \sum_{i+j \leq 2} \mathcal{M}_{\ell}^{(ij)} x^i y^j + \overline{m}_{\ell}^{(pg3)} \sum_{i+j \leq 2} \widetilde{\mathcal{P}}_{\ell}^{(ij)} x^i y^j \right] dA, \quad (8)$$

207 where $\widetilde{\mathcal{P}}_{\ell}^{(00)} = \mathcal{P}_{\ell}^{(00)} - \overline{\Delta p}_{\ell}^{(pg3)}$ and $\widetilde{\mathcal{P}}_{\ell}^{(ij)} = \mathcal{P}_{\ell}^{(ij)}$ for $i, j > 0$, and $\mathcal{M}_{\ell}^{(ij)}$ are the reconstruc-
 208 tion coefficients for the mixing ratio in CSLAM cell $A_{\ell}^{(pg3)}$. A shape-preserving limiter is
 209 applied to the reconstruction of mixing ratio m [*Barth and Jespersen*, 1989] and not Δp .
 210 This way of combining the reconstruction function for Δp and m in (8) ensures that a con-
 211 stant mixing ratio is preserved (consistency), tracer mass is conserved, linear-correlations
 212 are preserved and tracer shape-preservation is retained. The mixing ratio on the physics
 213 grid is then

$$\overline{m}_k^{(pg2)} = \frac{\overline{(m\Delta p)}_k^{(pg2)}}{\overline{\Delta p}_k^{(pg2)}}, \quad (9)$$

214 where $\overline{\Delta p}_k^{(pg2)}$ is given in (5).

215 Perhaps surprisingly a much more challenging problem is to map tracer increments
 216 (or state) from the physics grid to the CSLAM grid while retaining important properties
 217 such as mass-conservation, consistency, and correlation preservation. Why this mapping
 218 problem is challenging is explained in detail in Section 2.2.1 after having defined impor-
 219 tant properties for mapping physics increments/tendencies.

220 **2.2 Mapping tracer increments from $A^{(pg2)}$ to $A^{(pg3)}$ (physics to CSLAM grid)**

221 The increments from the parameterizations are computed on the physics grid. The
 222 tracer increment in physics grid cell k is denoted $\bar{f}_k^{(pg2)}$ so that the updated mixing ratio
 223 on the physics grid is $\bar{m}_k^{(pg2)} + \bar{f}_k^{(pg2)}$. The problem is how to map $\bar{f}_k^{(pg2)}$ to the CSLAM
 224 control volumes, to obtain $\bar{f}^{(pg3)}$, satisfying the following constraints:

- 225 1. **Local mass-conservation:** At a minimum total physics mass forcing on an element
 226 computed on the physics grid should equal the element physics mass forcing on the
 227 CSLAM grid

$$\bar{f}_k^{(pg2)} \bar{\Delta p}_k^{(pg2)} \Delta A_k^{(pg2)} = \sum_{\ell=1}^{nc^2} \left[\bar{\Delta p}_{\ell}^{(pg3)} \bar{f}_{\ell}^{(pg3)} \Delta A_{k\ell} \right], \quad (10)$$

228 where $\bar{\Delta p}_k^{(pg2)}$ is the pressure level thickness in physics grid cell k and similarly for
 229 $\bar{\Delta p}^{(pg3)}$. We enforce a more local constraint in which only mass-increments over-
 230 lapping with a particular CSLAM cell contributes to the mass-increment in that
 231 CSLAM cell.

- 232 2. **Local shape-preservation in mixing ratio:** The increments mapped to the CSLAM
 233 grid and added to the previous CSLAM state should not produce values smaller
 234 than the updated physics grid mixing ratios, $\bar{m}_k^{(pg2)} + \bar{f}_k^{(pg2)}$, or values smaller than
 235 the existing CSLAM mixing ratios that overlap with physics grid cell A_{ℓ}

$$\bar{m}_{\ell}^{(pg3)} + \bar{f}_{\ell}^{(pg3)} \geq \bar{m}_k^{(min)} = \min \left(\bar{m}_k^{(pg2)} + \bar{f}_k^{(pg2)}, \{ \bar{m}_{k\ell} | \ell = 1, nc^2 \} \right), \quad (11)$$

236 where

$$\bar{m}_{k\ell} = \frac{\langle m \delta p_{k\ell} \rangle}{\langle \delta p_{k\ell} \rangle}. \quad (12)$$

237 The numerator and denominator in (12) are defined in (6) and (8), respectively. In
 238 particular this means that an increment, when mapped to the pg3 grid, should not
 239 drive the state negative (described in detail below as the ‘negativity’ problem).
 240 A similar definition apply for maxima

$$\bar{m}_{\ell}^{(pg3)} + \bar{f}_{\ell}^{(pg3)} \leq \bar{m}_k^{(max)} = \max \left(\bar{m}_k^{(pg2)} + \bar{f}_k^{(pg2)}, \{ \bar{m}_{k\ell} | \ell = 1, nc^2 \} \right), \quad (13)$$

- 241 3. **Linear correlation preservation:** The physics forcing must not disrupt linear tracer
 242 correlation between species on the CSLAM grid [see, e.g., *Lauritzen and Thuburn*,
 243 2012], i.e. if two tracers are linearly correlated and the physics increment preserves
 244 linear correlations on the physics grid then the tracer increment on the CSLAM
 245 grid must not disrupt linear correlations.

246 **4. Consistency:** A non-zero constant mixing ratio increment from physics, $cnst$, on
 247 the physics grid, $\bar{f}_k^{(pg2)} = cnst \forall k$, must result in the same (constant) forcing on the
 248 CSLAM grid, $\bar{f}_\ell^{(pg3)} = \bar{f}_k^{(pg2)} = cnst \forall \ell$.

249 To motivate the algorithm that will simultaneously satisfy 1-4 it is informative to discuss
 250 how ‘standard’ mapping algorithms will violate one or more of the constraints:

251 **2.2.1 Why ‘conventional’ conservative remapping will not work**

252 It is helpful to analyze in detail why conventional remapping can not satisfy prop-
 253 erties 1-4 above. Assume that one remaps the mass-increments in exactly the same way
 254 as the mapping of mixing ratio state from the CSLAM grid to the physics grid described
 255 in section 2.1. That is, replace m with f and map from physics grid to the CSLAM grid
 256 instead of the other way around. Denote the mapped mass-increment $\widetilde{\bar{f}\Delta p}^{(pg3)}$ and due
 257 to the properties of the mapping algorithm the mass-increment is conserved, linear corre-
 258 lation between mass-increments are conserved and shape in mass-increment is preserved.
 259 The problems arise when converting from mass to mixing ratio.

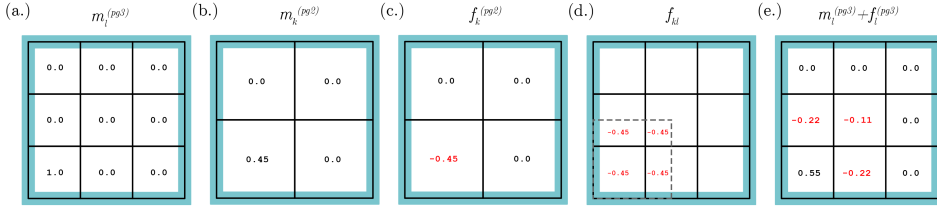
260 **2.2.1.1 Conserve mass but not consistency** If ones uses the known pressure-level
 261 thickness on the CSLAM grid $\bar{\Delta p}_k^{(pg3)}$ to convert from mass-increment to mixing-ratio
 262 increment

$$\bar{m}_k^{(pg3)} = \frac{\widetilde{\bar{f}\Delta p}_k^{(pg3)}}{\bar{\Delta p}_k^{(pg3)}}, \quad (14)$$

263 a constant mixing ratio increment is not conserved. Basically the constant increment mapped
 264 to the CSLAM grid and converted to mixing ratio increment through (14) will, rather
 265 than being constant, reflect the spurious discrepancy between $\widetilde{\bar{f}\Delta p}_k^{(pg3)}$ and $\bar{\Delta p}_k^{(pg3)}$, where
 266 $\widetilde{\bar{f}\Delta p}_k^{(pg3)}$ is the pressure-level thickness mapped from the pg2 grid to the pg3 grid. That
 267 said, mass will be conserved since the dynamical core state has $\bar{\Delta p}_k^{(pg3)}$ (unless the incre-
 268 ment drives the mixing ratio negative - described in detail below).

269 **2.2.1.2 Consistent but not mass-conserving** Rather than converting to mixing ratio
 270 using $\bar{\Delta p}_k^{(pg3)}$, a constant increment can be preserved by using

$$\bar{m}_k^{(pg3)} = \frac{\widetilde{\bar{f}\Delta p}_k^{(pg3)}}{\widetilde{\bar{\Delta p}}_k^{(pg3)}}, \quad (15)$$



274 **Figure 3.** Schematic illustration of the ‘negativity problem’ in a single element. (a.) Initial CSLAM tracer
275 values, (b.) mapped to pg2, (c) produces a tracer increment on pg2, (d.) with negative increments on the ex-
276 change grid overlying CSLAM cells in (a) that were initially zero and (e) driving those mixing ratios negative.

271 instead. But now mass-conservation is lost since, again, $\overline{\Delta p}_k^{(pg2)} \neq \overline{\Delta p}_k^{(pg2)}$. This issue
272 is similar to the mass-wind inconsistency found in specified dynamics applications [e.g.
273 *Jöckel et al., 2001; Lauritzen et al., 2011*].

277 **2.2.1.3 The ‘negativity’ problem and linear correlations** Even if one could derive
278 a reversible map for mapping $\overline{\Delta p}^{(pg2)}$ from the physics grid to the CSLAM grid, there
279 could still be problems if the increment drives the mixing ratios negative (or overshoot-
280 ing occurs) on the CSLAM grid. This can easily happen for tracers, such as cloud liquid
281 amount and cloud ice amount, that are zero in most of the domain and non-zero in local-
282 ized areas/points (where there are clouds). We refer to this as the ‘negativity problem’.
283 This problem is depicted schematically in Figure 3. Consider a single element of CSLAM
284 control volumes, containing only a single cell with mixing ratio 1.0, and 0.0 everywhere
285 else ($\overline{m}_\ell^{(pg3)}$; Figure 3a). The mixing ratios are mapped to the pg2 grid using, for sim-
286 plicity, the piecewise constant method where a constant value inside the pg2 cells is used
287 during the integration over overlap cells ($\overline{m}_k^{(pg2)}$; Figure 3b). Now consider the case in
288 which physics removes all the mass from the physics cell k : $\overline{f}_k^{(pg2)} = -\overline{m}_k^{(pg2)}$ (Figure 3c).
289 The tracer increment is mapped from pg2 to pg3 using the piecewise constant method.
290 Some of the non-zero increments are now in overlap areas where the original CSLAM
291 grid cells have mixing ratio zero ($\overline{f}_{k\ell}$; Figure 3d), and hence, the state is driven negative
292 when adding the overlap increment to the CSLAM state (Figure 3e). This is referred to as
293 the negativity problem although it can also happen for maxima.

The negativity issue could be avoided if one remaps the physics updated state instead of mapping increments/tendencies. In that case a shape-preserving filter will make sure that the state on the CSLAM grid is not negative (and does not overshoot). That said, if physics does not change the state and it is mapped back to the CSLAM grid then spurious tendencies (proportional to the errors introduced by mapping state from the CSLAM grid to the physics grid and back again) are introduced. Hence it is advantageous to map increments/tendencies since any reasonable algorithm will preserve a zero function.

As illustrated above a standard remapping method will NOT simultaneously satisfy 1-4 and hence a new algorithm has been derived.

2.3 New tendency mapping algorithm

The problem is how to map the mass-increment on the physics grid, $\bar{f}^{(pg2)} \Delta A^{(pg2)}$, to the CSLAM cells that overlap with $\Delta A^{(pg2)}$. To maintain shape-preservation, linear correlations and to avoid the negativity problem locally, it is advantageous to define a mass excess function on the exchange grid $\Delta m_{k\ell}^{(excess)}$. It is basically the maximum amount of mixing ratio that can be removed (in the case $\bar{f}^{(pg2)} < 0$) without producing new minima in the exchange grid mixing ratio $m_{k\ell}$

$$\Delta m_{k\ell}^{(excess)} = \bar{m}_{k\ell} - \bar{m}_k^{(min)}, \quad (16)$$

where $\bar{m}_{k\ell}$ is defined in (12). So the maximum amount of mass that we can be removed from the exchange grid cells that span physics grid cell A_k without violating the shape-preservation constraint ((11) and (13)) is

$$\sum_{\ell} \Delta m_{k\ell}^{(excess)} \bar{\Delta p}_{k\ell} \delta A_{k\ell}. \quad (17)$$

If physics is designed not to remove more mass than available in A_k (which should be the case for a carefully designed physics package) then it is guaranteed that

$$\sum_{\ell} \Delta m_{k\ell}^{(excess)} \bar{\Delta p}_{k\ell} \delta A_{k\ell} \geq \bar{f}^{(pg2)} \Delta p_k \Delta A^{(pg2)}. \quad (18)$$

We distribute the physics mass-forcing (assuming $\bar{f}^{(pg2)} < 0$) according to the mass excess in each overlap area by solving this equation for γ_k

$$\Delta A_k^{(pg2)} \bar{\Delta p}_k^{(pg2)} \bar{f}^{(pg2)} = \gamma_k \sum_{\ell} \Delta m_{k\ell}^{(excess)} \bar{\Delta p}_{k\ell} \delta A_{k\ell}, \quad (19)$$

and add mass increment (which in this case is negative)

$$\gamma_k \Delta m_{k\ell}^{(excess)} \bar{\Delta p}_{k\ell} \delta A_{k\ell}, \quad (20)$$

318 to the ℓ th CSLAM cell state $\overline{m}^{(pg3)} \overline{\Delta p}_\ell^{(pg3)} \Delta A_\ell^{(pg3)}$. This process is repeated for all physics
 319 cells. Note that this problem is a well-posed, i.e. $\gamma_k > 0$, since physics will not remove
 320 more mass than is locally available (18). The way in which the mass-forcing is distributed
 321 to the CSLAM cells using the excess function insures that the negativity problem is avoided.
 322 Mass is conserved by design and shape-preservation is obtained by using the excess func-
 323 tion.

324 If the physics increment is positive (assuming $\overline{f}^{(pg2)} > 0$) we define a ‘lack’ function

$$\Delta m_{k\ell}^{(lack)} = \overline{m}_{k\ell} - \overline{m}^{(max)}, \quad (21)$$

325 and solve

$$\overline{\Delta p}_k^{(pg2)} \overline{f}^{(pg2)} \Delta A_k^{(pg2)} = \gamma_k \sum_\ell \left[\Delta m_{k\ell}^{(lack)} \overline{\Delta p}_{k\ell} \delta A_{k\ell} \right], \quad (22)$$

326 for γ_k and follow the same procedure as for mass excess. Since positive and negative forc-
 327 ing is treated in exactly the same way, linear correlations are preserved. Note how the def-
 328 initition of the excess/lack function insures linear correlation preservation; for example, if
 329 one would prevent negative values and not do anything about overshoots then linear corre-
 330 lations would not be preserved since the minima and maxima are not treated in the same
 331 way.

332 While the above algorithm satisfies properties 1-4 in section 2.2, it is not a high-
 333 order algorithm in terms of formal accuracy. This is illustrated in Figure 4 (row 3) where
 334 a smooth analytical tendency [approximate spherical harmonic of order 32 and azimuthal
 335 wave number 16; *Jones, 1999*]

$$f^{(pg2)} = \frac{1}{2} + \frac{1}{2} \cos(16\lambda) \sin(2\theta)^{16}, \quad (23)$$

336 where (λ, θ) is latitude-longitude, is mapped from $pg2$ to $pg3$ grid using this algorithm
 337 assuming $m_\ell^{(pg3)} = 0, \forall \ell$. The errors in the mapping are not always aligned with large
 338 gradients in the analytical function as would be expected for a ‘traditional’ interpolation
 339 algorithm. The errors are maximum on the order of 60%. To reduce errors we therefore
 340 perform a higher-order pre-allocation of tendencies that is not mass-conserving but satis-
 341 fies properties 2,3, and 4 in Section 2.2.

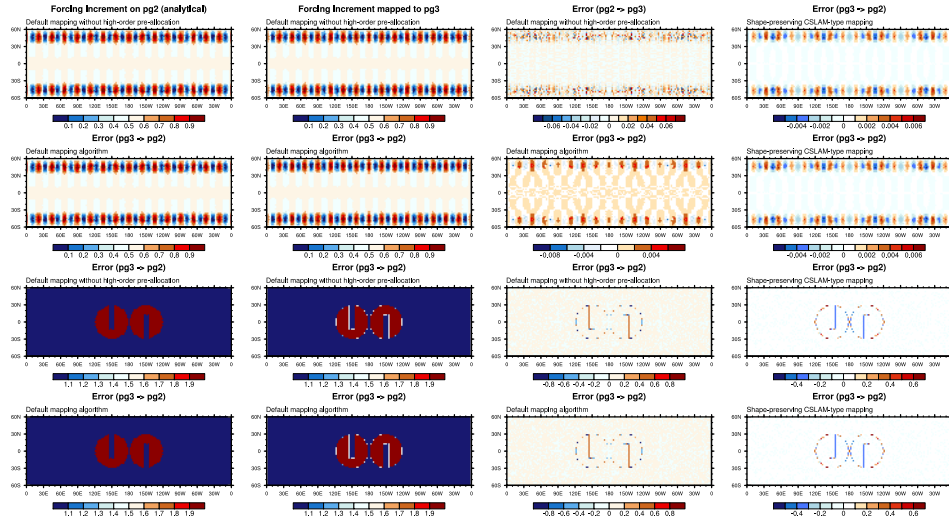


Figure 4. Mapping of idealized functions from $pg2$ (column 1) to $pg3$ (columns 2 and 3) and errors (column 4) using the new tendency algorithm only (row 1 and 3) and new tendency algorithm with the high-order pre-allocation (row 2 and 4). Column 4 shows the errors in mapping the same distributions from $pg3$ to $pg2$ using traditional remapping (CSLAM technology).

2.4 High-order (non-conservative) pre-allocation of tracer tendencies

A high-order tracer mass increment in overlap area $A_{k\ell}$ can be computed using the following formula

$$\langle f \delta p \rangle_{k\ell} = \int_{A_{k\ell}} \left[\overline{\Delta p}_{\ell}^{(pg3)} \sum_{i+j \leq 2} \mathcal{F}_k^{(ij)} x^i y^j + \overline{f}_k^{(pg2)} \sum_{i+j \leq 2} \widetilde{\mathcal{P}}_{\ell}^{(ij)} x^i y^j \right] dA, \quad (24)$$

where $\mathcal{F}_k^{(ij)}$ is the forcing increment reconstruction coefficients in the k th physics grid cell and $\overline{f}_k^{(pg2)}$ is the average physics increment in the k th physics grid cell. Note that we are using the known dry pressure reconstruction coefficients on the $pg3$ grid instead of reconstructing sub-grid-scale pressure variations from the physics grid cell averaged values. We can do that since the dry pressure is not modified by physics. This highlights the importance of a dry-pressure formulation of the dynamical core when separating physics and dynamics grids [Lauritzen *et al.*, 2018]. If the physics forcing is constant then $\langle f \delta p \rangle_{k\ell}$ exactly equals $\langle \delta p \rangle_{k\ell}$ from (6); in other words, the mapping is designed to be reversible in dry pressure. The physics increment in terms of mixing ratio change is given by

$$\overline{f}_{k\ell} = \frac{\langle f \delta p \rangle_{k\ell}}{\langle \delta p \rangle_{k\ell}}, \quad (25)$$

where the denominator is given by (6).

359 Shape-preservation, as defined by (11) and (13), is enforced by eliminating under
 360 and overshoots on the exchange grid by modifying the forcing increment $\bar{f}_{k\ell}$ so that shape-
 361 preservation is not violated in the overlap areas¹

$$\bar{m}_k^{(min)} \leq \bar{m}_{k\ell} + \tilde{\bar{f}}_{k\ell} \leq \bar{m}_k^{(max)}. \quad (27)$$

362 While this algorithm preserves linear correlations, shape, and is consistent, is it not mass-
 363 conservative. Hence the remaining physics increment not allocated in the algorithm above
 364 is allocated using the new tendency algorithm described in Section 2.3.

365 Combining the high-order pre-allocation algorithm with the new tendency algo-
 366 rithm (which in this case can also be considered as a mass-fixer that does not disrupt
 367 correlation-preservation, shape and consistency) leads to an order-of-magnitude reduction
 368 in mapping errors for a smooth function (see Figure 4 row 3 and 4) while full-filling the
 369 mass-conservation, shape-preservation, linear correlation and consistency constraint. Mass
 370 and linear correlation preservation is illustrated in the baroclinic wave test with termina-
 371 tor chemistry test in Section 3.1. Shape-preservation and consistency is demonstrated in
 372 an idealized mapping test where a smooth function, see (23), and a slotted-cylinder [see
 373 equation 12 in *Lauritzen et al., 2012*] are mapped to/from the *pg2* and *pg3* grids. Since
 374 the background value in the mapping of the slotted-cylinder field is preserved the mapping
 375 algorithm is consistent. Since no new over- and undershoots are produced (particularly ob-
 376 vious in the mapping of the slotted cylinders) the mapping is shape-preserving. We also
 377 note that the mapping errors with the default algorithm (higher-order pre-allocation with
 378 new tendency algorithm) are similar to the errors in mapping the same field from *pg3* to
 379 *pg2* using traditional remapping with CSLAM technology (column 4 in Figure 4).

380 2.5 Model Configurations

381 All simulations in this study are run on the Cheyenne supercomputer hosted at the
 382 NCAR-Wyoming Supercomputer Center [*Computational and Information Systems Lab-*
 383 *oratory, 2017*]. Three model component sets (*compsets*) in the Community Earth Sys-

¹ In the computation of $\bar{m}_{k\ell}$ there can be small overshoots and undershoots (due to numerical integration errors) com-
 pared to the CSLAM cell average values $\bar{m}_\ell^{(pg3)}$ that it overlaps with so we set

$$\bar{m}_k^{(min)} = \min \left(\bar{m}_k^{(min)}, \left\{ \bar{m}_\ell^{(pg)} \mid \ell = 1, nc^2 \right\} \right) \quad (26)$$

384 tem Model, version 2.1 (CESM2.1; <https://doi.org/10.5065/D67H1H0V>) are cho-
 385 sen to carry out the objectives discussed in Section 1. The least complex compset is a
 386 moist baroclinic wave test using a simple, Kessler microphysics scheme [*FKESSLER*
 387 compset; *Lauritzen et al.*, 2018]. The baroclinic wave setup is primarily used to evaluate
 388 the new mapping algorithms and their ability to preserve linear-correlations between two
 389 reactive tracers. The role of topography is investigated using a dry Held-Suarez config-
 390 uration [*FHS94* compset; *Held and Suarez*, 1994] modified to include real world topog-
 391 raphy. H18 indicate that this configuration tends to have more grid-noise over steep ter-
 392 rain than in a more complex configuration using CAM, version 6 physics [CAM6; https://ncar.github.io/CAM/doc/build/html/users_guide/index.html], and is there-
 393 fore a conservative choice for evaluating any change in grid imprinting between *pg3* and
 394 *pg2*.
 395

396 To understand whether the resolved scales of motion are influenced by a coarser res-
 397 olution physics grid, a suite of aqua-planet simulations [*Neale and Hoskins*, 2000; *Medeiros*
 398 *et al.*, 2016] are carried out over a range of spectral-element grid resolutions, using CAM6
 399 physics (*QPC6* compset). The aqua-planet is an ocean covered planet in perpetual equinox,
 400 with fixed, zonally-symmetric sea surface temperatures idealized after present day Earth
 401 [*QOBS* in *Neale and Hoskins*, 2000]. While the dynamics time-step, Δt_{dyn} , varies with
 402 resolution according to a CFL criterion, there is no established standard for how the physics
 403 time-step, Δt_{phys} , should vary across resolutions. This is further complicated by several
 404 studies indicating a high sensitivity of solutions to Δt_{phys} in CAM [*Williamson and Olson*,
 405 2003; *Williamson*, 2013; *Wan et al.*, 2015; *Herrington and Reed*, 2018].

406 Here, a scaling for Δt_{phys} across resolutions is proposed, based on results of the
 407 moist bubble test [*Herrington and Reed*, 2018] using CAM-SE-CSLAM and detailed in
 408 Appendix A: . The basis for the scaling is to alleviate truncation errors that arise in the
 409 moist bubble test when Δt_{phys} is too large. The scaling is linear in grid-spacing,

$$\Delta t_{phys} = \Delta t_{phys,0} \times \frac{N_{e,0}}{N_e} s, \quad (28)$$

410 where $\Delta t_{phys,0}$ is taken to be the standard 1800s used in CAM-SE-CSLAM at low reso-
 411 lution, $N_{e,0} = 30$ (equivalent to a dynamics grid-spacing of 111.2km). N_e refers to the
 412 horizontal resolution of the grid; each of the six panels of the cubed-sphere are divided
 413 into $N_e \times N_e$ elements. Throughout the paper, spectral-element grid resolutions are denoted
 414 by an *ne* followed by the quantity N_e , e.g., *ne30*.

The only other parameter varied across resolutions modulates the strength of explicit numerical dissipation. The spectral element method is not implicitly diffusive, so fourth-order hyper-viscosity operators are applied to the state to suppress numerical artifacts. The scaling of the hyper-viscosity coefficients, ν , across resolutions is defined as,

$$\nu_T = \nu_{vor} = 0.30 \times \left(\frac{30}{N_e} 1.1 \times 10^5 \right)^3 \frac{m^4}{s}, \quad (29)$$

$$\nu_p = \nu_{div} = 0.751 \times \left(\frac{30}{N_e} 1.1 \times 10^5 \right)^3 \frac{m^4}{s}, \quad (30)$$

where subscripts T , vor , p , div refer to state variables the operators are applied to, temperature, vorticity, pressure and divergence, respectively. The exponent in equation (30) reduces the coefficient by about² an order of magnitude for each doubling of the resolution [as in *Lauritzen et al.*, 2018]. No explicit dissipation of tracers (e.g., water vapor) is required since the semi-Lagrangian numerics in CSLAM are diffusive.

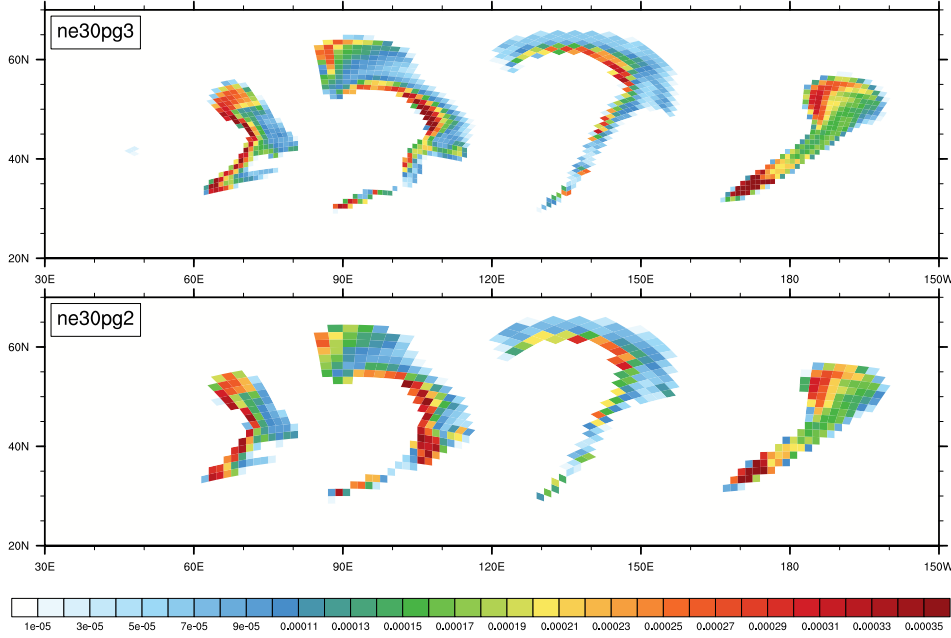
3 Results

3.1 Mass Conservation and Linear-Correlation Preservation

To illustrate how different the solutions look using the coarser resolution physics grid, Figure 5 shows a snapshot of the cloud liquid field of the moist baroclinic wave test on day 10, in the *ne30pg3* and *ne30pg2* configurations. The cloud liquid fields show in detail clouds forming at wave fronts. As expected, the *pg2* grid looks slightly coarser than *pg3* due to its larger control volumes. Despite this, the details of the wave patterns look reasonably similar to one another.

The models ability to preserve linear correlations is assessed using the idealized Terminator "Toy" Chemistry test [*Lauritzen et al.*, 2015a, 2017]. The tests consists of two reactive species undergoing photolysis as they are advected over the terminator line. The flow field is provided by the moist baroclinic waves test. The model is initialized with species such that their weighted sum Cly is a constant, i.e., $Cly = Cl + 2Cl_2 = 4 \times 10^{-6}$ kg kg⁻¹. If linear-correlations are preserved, than the column integrated weighted sum of the species, $\langle Cly \rangle$, is constant.

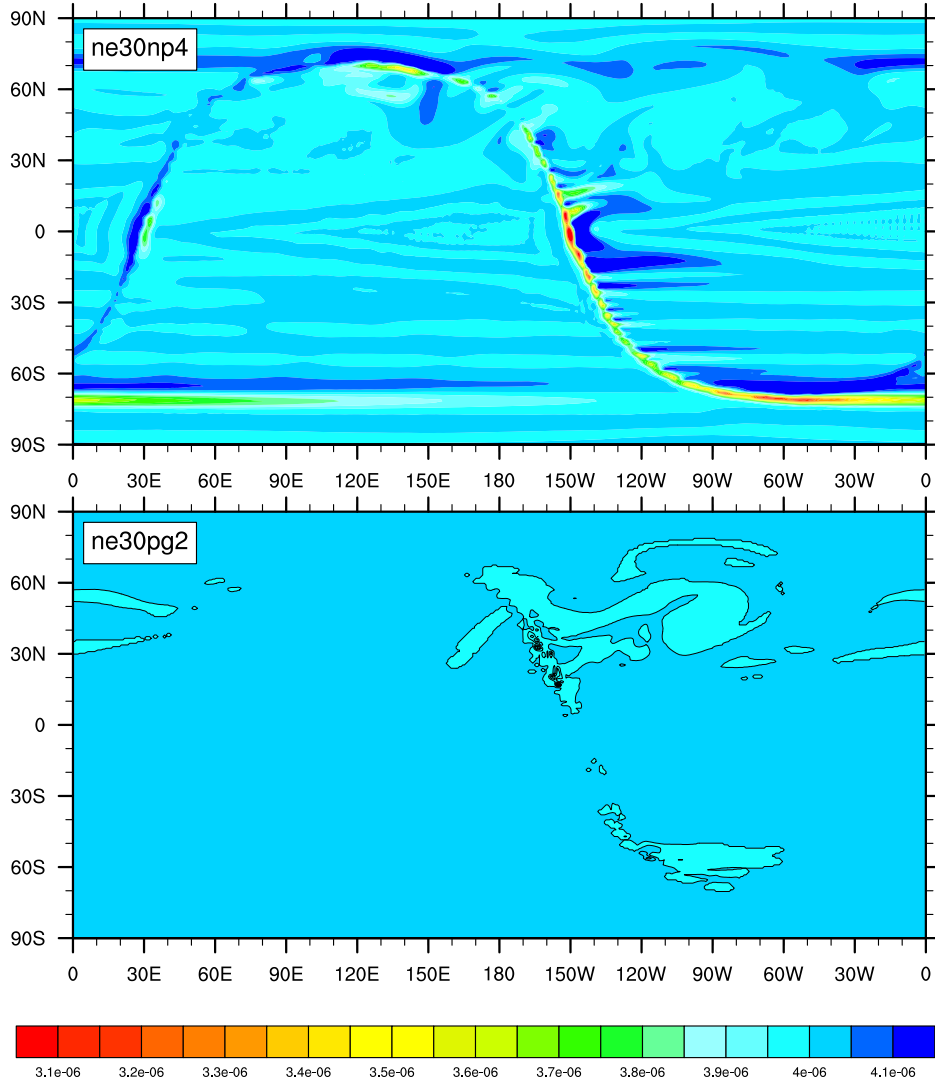
² This is approximate. To reduce the coefficients by exactly an order of magnitude for each doubling of the resolution, the exponent should be $\frac{\ln 2}{\ln 10} \approx 3.01029$, which it has been updated to in the most recent version of CESM2.1



428 **Figure 5.** Snapshot of the cloud liquid field in kg kg^{-1} near the 700hPa level, on day 10 of the moist
 429 baroclinic wave test in the *ne30pg3* and *ne30pg2* configurations, displayed on the upper and lower panels,
 430 respectively. The fields are shown as a raster plot on their respective physics grids.

441 H18 had shown that in the *ne30pg3* configuration, $\langle CLy \rangle$ on day 15 of the termin-
 442 inator test is everywhere $4 \times 10^{-6} \text{ kg kg}^{-1}$, to within machine precision. While the *pg3* to
 443 *pg2* mapping algorithm in theory preserves linear correlations to machine precision, we
 444 found larger than round-off errors in *pg2*, likely due to *if*-logic with machine dependent
 445 thresholds in the implementation of the algorithm. Figure 6 shows $\langle CLy \rangle$ on day 15 in
 446 the *ne30pg2* configuration, which has a minimum value of $3.99936 \times 10^{-6} \text{ kg kg}^{-1}$, cor-
 447 responding to a maximum relative error of 0.016%. For comparison, another terminator
 448 test is performed with the equivalent dynamics grid resolution using CAM-SE (*ne30np4*),
 449 in which tracers are advected using the spectral element method. The maximum rela-
 450 tive error in this configuration is 31.6%, three orders of magnitude greater error than the
 451 *ne30pg2* configuration.

452 Tracer mass conservation is analyzed in a pair of *ne30pg2* and *ne30pg3* aqua-planet
 453 simulations, following the method of *Lauritzen and Williamson* [2019]. Energy and mass
 454 conservation due to a particular model process is assessed by model state I/O before and
 455 after each sub-process in the model. The loss of water vapor mass due to the mapping



438 **Figure 6.** $\langle CLy \rangle$ in kg kg^{-1} on day 15 of the moist baroclinic wave test in the *ne30np4* and *ne30pg2* con-
 439 figurations, displayed on the upper and lower panels, respectively. The lower panel has a single contour level
 440 of $3.999E-6 \text{ kg kg}^{-1}$ corresponding to a relative error of 0.025%.

456 algorithms in the *ne30pg2* configuration is estimated as $1.184E-16 \text{ Pa}$ per time-step, com-
 457 puted as the difference between the the column integrated, global mean climatological wa-
 458 ter vapor pressure increment on the physics grid and on the tracer grid. This small error
 459 is effectively zero to within machine precision, and similar to an equivalent calculation in
 460 the *ne30pg3* simulation of $2.171E-17 \text{ Pa}$ per time-step, which contains no mapping er-
 461 rors since the physics and tracer grids coincide. Negligible mapping error in the *ne30pg2*
 462 configuration is primarily a result of solving equations (19),(22) for γ_k to circumvent the

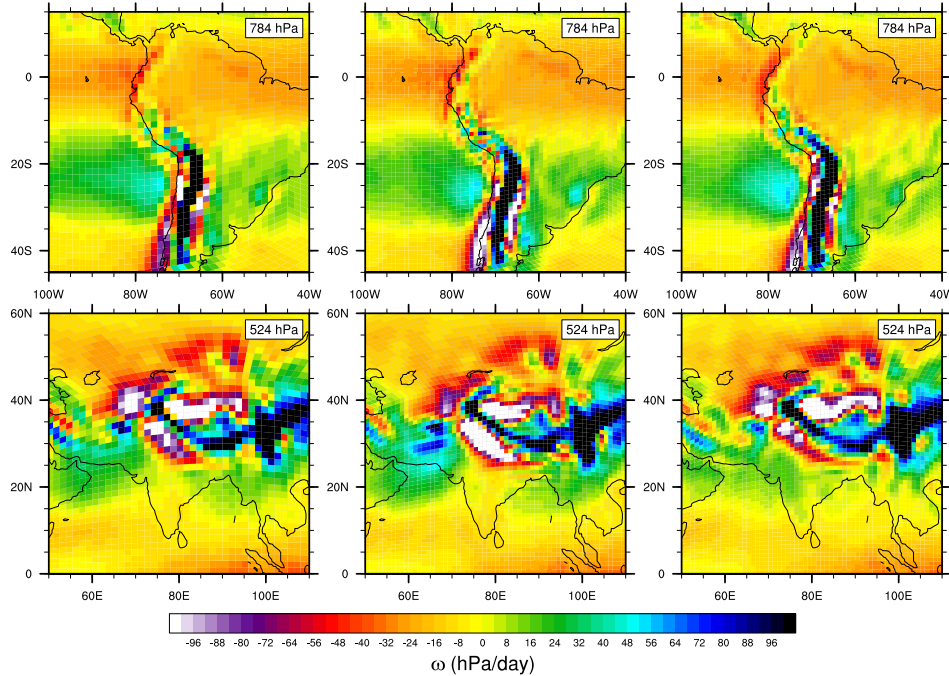
463 ‘negativity’ problem. Re-running the *ne30pg2* aqua-planet simulation without this mass
 464 fixer, e.g., through setting $\gamma_k = 1$ and $\Delta m_{k\ell}^{(excess)} = \bar{m}_{k\ell}$ in the mass increment (20), results
 465 in a spurious loss of water vapor mass of 2.424E–07 Pa per time-step; the mass fixer is
 466 necessary for conserving tracer mass in *ne30pg2*.

467 3.2 Grid Imprinting

468 Flow over topography can result in significant grid imprinting using the spectral ele-
 469 ment method [Lauritzen *et al.*, 2015b, H18]. Figure 7 shows the results of the Held-Suarez
 470 with topography simulations. The middle panel is the vertical pressure velocity, ω , aver-
 471 aged over two years, over the Andes and Himalayan region at two different levels in the
 472 mid-troposphere, using the *ne30pg3* grid. The fields are displayed as a raster plot on the
 473 physics grid, so that individual extrema, which characterize the flow over the Andes be-
 474 tween about 10° – 20° S, may be identified as spurious. Near the foot of the Himalayas,
 475 between about 20° – 30° N, there are parallel stripes of extrema aligned with the mountain
 476 front that appear to be spurious $2\Delta x$ oscillations.

481 As discussed in H18, grid imprinting over mountainous terrain tends to occur in re-
 482 gions of weak gravitational stability, causing extrema to extend through the full depth of
 483 the troposphere as resolved updrafts and downdrafts. Thus, grid imprinting over mountains
 484 may be alleviated through increasing the divergence damping in the model. Figure 7 (right
 485 panel) repeats the *ne30pg3* simulation through increasing ν_{div} by an order of magnitude.
 486 The spurious noise over the Andes and the Himalayas are damped, and grid point extrema
 487 tend to diffuse into neighboring grid cells. The wavenumber-power spectrum of the ki-
 488 netic energy due to divergent flow (Figure 8) confirms that divergent modes are damped
 489 at higher wavenumbers (greater than 30), by about an order of magnitude relative to the
 490 default *ne30pg3* simulation.

494 The ω field of the *ne30pg2* simulation is provided in Figure 7 (left panel). Grid cell
 495 extrema over the Andes is less prevalent than in the *ne30pg3* simulation, as seen by the
 496 reduction in large magnitude ω (e.g., red grid cells). The spurious oscillations at the foot
 497 of the Himalayas appear to have been entirely eliminated. This improvement in grid im-
 498 printing is due to the consistent smoothness properties of the control volumes in the *pg2*
 499 grid compared with the *pg3* grid discussed in Section 1, and these results are consistent
 500 with our hypothesis. The divergent modes are marginally damped relative to *ne30pg3* for

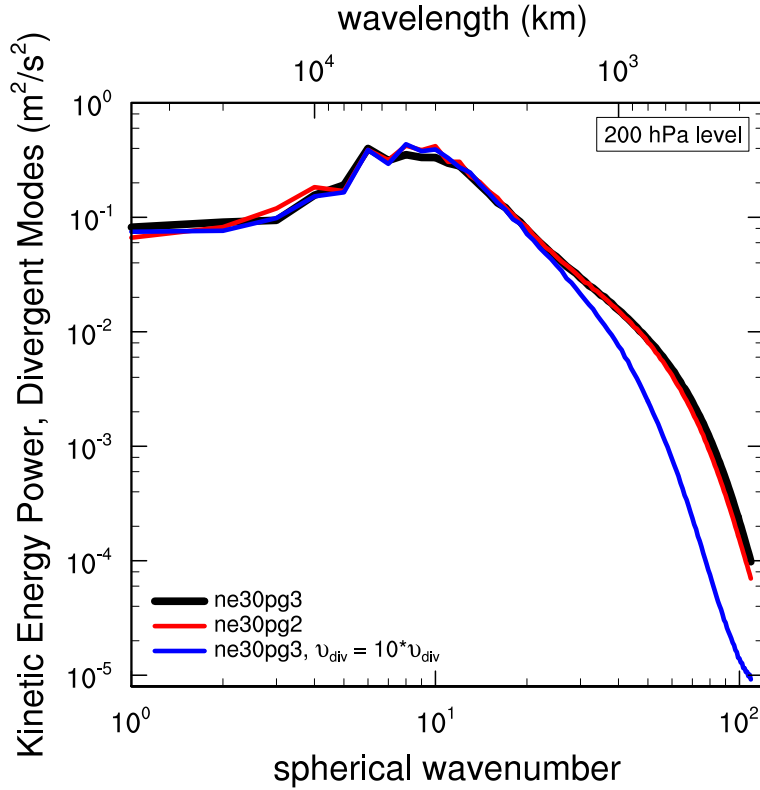


477 **Figure 7.** Mean ω at two model levels in the middle troposphere, in a Held-Suarez configuration outfitted
 478 with real world topography. (Left) *ne30pg2* (Middle) *ne30pg3* and (Right) *ne30pg3* with the divergence
 479 damping coefficient, ν_{div} , increased by an order of magnitude. The ω fields are computed from a two-year
 480 simulation. The data are presented on a raster plot in order to identify individual grid cells

501 wavenumbers greater than about 50, but are an order of magnitude larger than in the en-
 502 hanced divergence damping *ne30pg3* run (Figure 8). From a scientific and model devel-
 503 opment perspective, the *pg2* configuration is preferable to the *pg3* configuration, since it
 504 eliminates grid imprinting without placing any additional constraints on ν_{div} .

505 3.3 Impact on Resolved Scales of Motion

506 Tropical regions are very sensitive to horizontal resolution, primarily due to the
 507 scale dependence of resolved updrafts and downdrafts at hydrostatic scales [Weisman *et al.*,
 508 1997; Pauluis and Garner, 2006; Jeevanjee, 2017; Herrington and Reed, 2017, 2018]. The
 509 vertical velocity of updrafts and downdrafts is related to the horizontal length scales of
 510 buoyancy the model is able to support. This can be demonstrated through a scale analysis
 511 of the Poisson equation [Jeevanjee and Romps, 2016] valid for hydrostatic scales, showing



491 **Figure 8.** Kinetic energy power spectrum arising from divergent modes in *ne30pg3*, *ne30pg2* and *ne30pg3*
492 with the divergence damping coefficient, v_{div} , increased by an order of magnitude, in the Held-Suarez with
493 topography simulations. Spectra computed from five months of six-hourly winds.

512 that the ratio of the scale of ω at two resolutions, due to their respective buoyancies is,

$$\frac{\omega_{\Delta x_1}}{\omega_{\Delta x_2}} = \frac{D_{\Delta x_2}}{D_{\Delta x_1}}, \quad (31)$$

513 where $D_{\Delta x}$ is a characteristic buoyancy horizontal length scale for grid-spacing Δx (here-
514 after referred to as the *forcing scale*), and it is presumed that the magnitude of the buoy-
515 ancy and the vertical scale of the buoyancy is unchanged or compensating across the two
516 resolutions. Equation (31) indicates that the magnitude of the vertical velocity scales like
517 the inverse of the forcing scale, which was verified in a simple moist bubble configuration
518 using CAM-SE and the CAM finite-volume dynamical core [Herrington and Reed, 2018],
519 as well as using CAM-SE-CSLAM as configured in the present study (Appendix A:). It
520 is by no means trivial that equation (31) holds for the moist bubble test, since the scaling
521 is derived from the dry anelastic equations.

522 In aqua-planet simulations using CAM-SE, the forcing scale is grid-limited, varying
 523 with resolution in the range of five to ten times the grid-spacing [Herrington and Reed,
 524 2018]. From equation (31), this grid-dependence explains why the updrafts and down-
 525 drafts are so sensitive to horizontal resolution. A grid-limited forcing scale is analogous
 526 to an effective resolution, which is the characteristic length scale below which the solution
 527 becomes contaminated by numerical artifacts, and the features are overly damped due to
 528 numerical dissipation. The effective resolution may be inferred from kinetic energy spectra
 529 as the wavenumber where the slope of the spectrum becomes steeper than the observation-
 530 ally determined slope [Skamarock, 2011]. In the CESM2 release of CAM-SE, this crite-
 531 rion occurs near wavenumber 60 [see Figure 6 in Lauritzen *et al.*, 2018], a length scale of
 532 about six times the grid spacing and overlapping with the estimated forcing scale.

533 When the physics and dynamics grids are of different resolutions, which grid de-
 534 termines the models characteristic forcing scale? The remainder of Section 3 attempts to
 535 address this question using spectral element grids at low resolution (Section 3.3.1), high
 536 resolution (Section 3.3.2) and across all resolutions typical of present day climate models
 537 (Section 3.3.3).

538 3.3.1 Low Resolution

539 The question posed above may be addressed through comparing *ne30pg2*, where
 540 $\Delta x_{phys} = 166.8\text{km}$ (hereafter Δx is expressed as the average equatorial grid spacing), $\frac{3}{2}$
 541 times larger than the dynamics grid spacing, $\Delta x_{dyn} = 111.2\text{km}$, to a simulation where
 542 both are equal to the physics grid spacing, $\Delta x_{dyn} = \Delta x_{phys} = 166.8\text{km}$ (*ne20pg3*), and
 543 another simulation where both are equal to the dynamics grid spacing, $\Delta x_{dyn} = \Delta x_{phys} =$
 544 111.2km (*ne30pg3*). The resolvable scales in the *ne30pg2* solution are expected to be
 545 bounded by the *ne20pg3* and *ne30pg3* solutions. Although according to equation (28),
 546 Δt_{phys} for *ne20* grids should be different from *ne30* grids, here it is set to the *ne30* value
 547 (see Table 1) in order to reduce the differences between the three configurations, and
 548 justified because lower resolution runs aren't very sensitive to this range of Δt_{phys} (Fig-
 549 ure A.2).

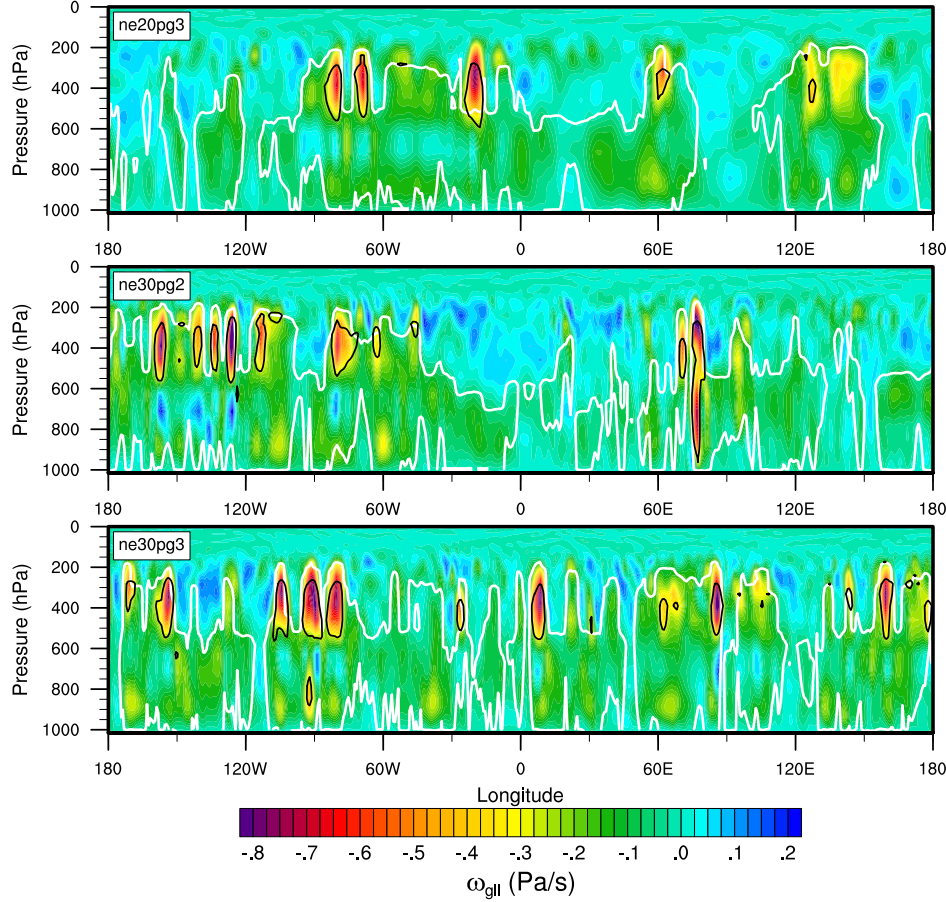
552 Figure 9 is a snapshot of the ω field in the Inter-Tropical Convergence Zone (ITCZ)
 553 in the pressure-longitude plane, in the three simulations. The ω field is overlaid with the
 554 $\pm 15K/day$ contour of the physics temperature tendencies (black), which are primarily

550 **Table 1.** Δx and Δt for the physics and dynamics in the low resolution simulations. Δx is computed as the
 551 average equatorial grid spacing.

Grid name	Δx_{dyn}	Δt_{dyn}	Δx_{phys}	Δt_{phys}
ne20pg3	166.8km	300s	166.8km	1800s
ne30pg2	111.2km	300s	166.8km	1800s
ne30pg3	111.2km	300s	111.2km	1800s

555 due to stratiform cloud formation. Since the component of ω due to buoyancy is deter-
 556 mined by the physics temperature tendencies mapped to the GLL grid, the tendencies
 557 and ω are shown on the *GLL* grid, $f_T^{(gll)}$ and $\omega^{(gll)}$, respectively. The white contour is
 558 intended to outline regions where the deep convection scheme is fairly active, set to the
 559 $0.0075\text{kg/m}^2/\text{s}$ value of the convective mass fluxes (note the convective mass fluxes have
 560 not been mapped to the *GLL* grid, and are instead shown on the *pg* grid). The figure in-
 561 dicates that large regions of the ITCZ are comprised of upward ω that balance the warm-
 562 ing due to compensating subsidence produced by the deep convection scheme. Much
 563 larger magnitude ω are comprised of resolved updrafts driven by the buoyancy of strati-
 564 form clouds, and resolved downdrafts due to evaporation of condensates produced by over-
 565 lying clouds [Herrington and Reed, 2018]. These large buoyancy stratiform clouds tend
 566 to form in the middle-to-upper troposphere due to detrainment of moisture from the deep
 567 convection scheme [Zhang and McFarlane, 1995].

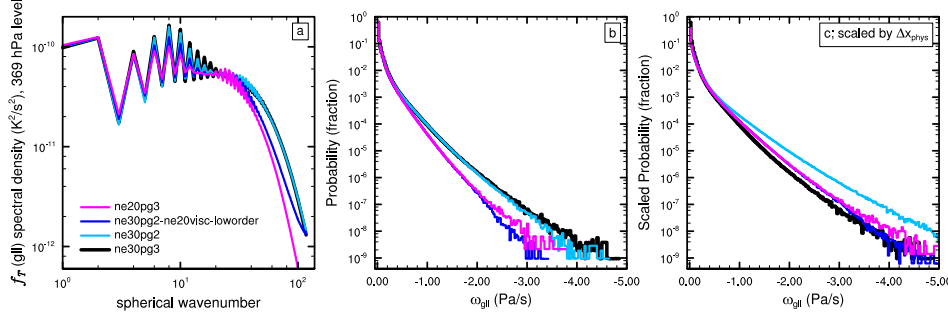
572 It is not obvious from the snapshots in Figure 9 whether the length scales of the
 573 stratiform clouds, which are approximately equal to the models characteristic forcing scale,
 574 are any different across the three simulations. Analogous to determining the effective reso-
 575 lution [Skamarock, 2011], the forcing scale may be inferred from the wave-number power
 576 spectrum of $f_T^{(gll)}$ as the maximum wavenumber prior to the steep, un-physical decline in
 577 power that characterizes the near-grid scale (hereafter $f_T^{(gll)}$ is referred to as the *forcing*).
 578 The wave-number power spectrum of the forcing in the middle-to-upper troposphere is
 579 shown in Figure 10a. Unlike kinetic energy spectra, the decline in power near the mod-
 580 els effective resolution is more gradual, making it difficult to determine a characteristic
 581 forcing scale from the spectra. However, it is clear that the slope of the *ne20pg3* spec-
 582 trum begins to steepen at smaller wavenumbers than in the *ne30pg3* spectra. Additionally,



568 **Figure 9.** Snapshots in the longitude-pressure plane of $\omega^{(gll)}$ through the ITCZ region in the *ne20pg3*,
 569 *ne30pg2* and *ne30pg3* configurations, in the upper, middle and lower panels, respectively. Black is the
 570 $\pm 15\text{K}/\text{day}$ contour of the physics tendencies, and the white contour is the $0.0075\text{kg}/\text{m}^2/\text{s}$ contour of the
 571 parameterized deep convective mass fluxes.

583 the *ne30pg2* spectra is remarkably similar to the *ne30pg3* spectra, for all wavenumbers.
 584 These spectra indicate that the characteristic forcing scale in the *ne30pg2* and *ne30pg3*
 585 simulations are similar, and that both are smaller than the *ne20pg3* forcing scale. From
 586 equation (31), it is expected that the magnitude of the vertical motion is greater in both
 587 the *ne30pg2* and *ne30pg3* simulations.

592 The probability density function (PDF) of upward $\omega^{(gll)}$ everywhere in the simula-
 593 tions is shown in Figure 10b. Large magnitude $\omega^{(gll)}$ are more frequent in the *ne30pg2*
 594 run, compared to *ne20pg3*, and the PDF is actually more similar to the *ne30pg3* distribu-
 595 tion, consistent with their similar forcing scales. This may be further illustrated through



588 **Figure 10.** (Left) Wavenumber-power spectrum of the temperature tendencies from the moist physics,
 589 near the 369 hPa level, (Middle) probability density distribution and (Right) the scaled probability density
 590 distribution of upward ω everywhere in the model. The scaled distributions are scaled to *ne30pg3* using
 591 Δx_{phys} .

596 scaling the PDF's,

$$P_s(\omega) = \alpha \times P(\omega/\alpha), \quad (32)$$

597 where $P_s(\omega)$ is the scaled PDF of ω and α is the ratio of ω to ω_{target} , the ω associated
 598 with the target grid resolution, Δx_{target} . Making the assumption that the forcing scale is
 599 linear in Δx , then from equation (31), $\alpha = \Delta x_{target}/\Delta x$. The target resolution is taken
 600 here to be equal to the *ne30pg3* grid resolution.

601 If the forcing scale of *ne30pg2* is in fact determined by Δx_{phys} , then one sets $\Delta x =$
 602 Δx_{phys} in α . This scaled PDF, however, severely overestimates the frequency of upward
 603 ω of the target resolution, *ne30pg3* (Figure 10c). It is clear from the similarity of the
 604 un-scaled PDF's of *ne30pg2* and *ne30pg3* (Figure 10b), and their forcing spectra (Fig-
 605 ure 10a), that the characteristic forcing scale in these two configurations are approximately
 606 the same. It follows that the forcing scales in *ne30pg2* and *ne30pg3* are determined by
 607 their common grid, Δx_{dyn} , rather than Δx_{phys} , which are different. And one can be rea-
 608 sonably confident in the linear framework used to approximate α - the scaled *ne20pg3*
 609 PDF fits the *ne30pg3* distribution quite well. It then follows that the forcing scale of *ne20*
 610 simulations is about $\frac{3}{2}$ times that of *ne30* simulations, the ratio of their grid spacings.

611 There are two reasons the *pg2* forcing scale is determined by the *GLL* grid. The
 612 first being that the hyper-viscosity coefficients are a function of the *GLL* grid resolution
 613 (equation (30)), and the second, that the physics tendencies are mapped to the *pg3* and
 614 *GLL* grids using high-order mapping, which reconstructs scales the *pg2* grid is unable to

633 **Table 2.** Δx and Δt for the physics and dynamics in the high resolution simulations. Δx is computed as the
 634 average equatorial grid spacing.

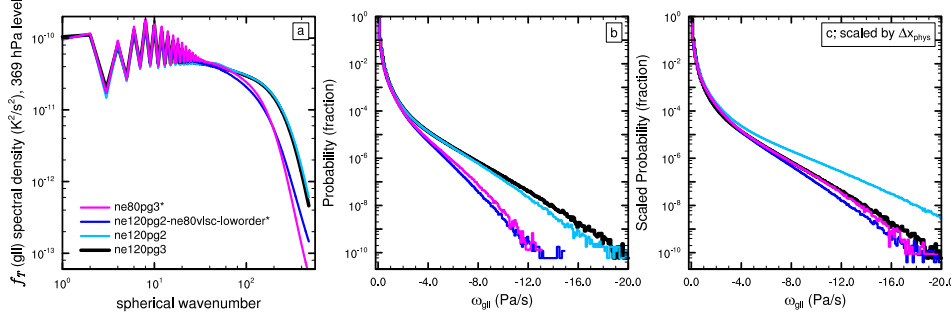
Grid name	Δx_{dyn}	Δt_{dyn}	Δx_{phys}	Δt_{phys}
ne80pg3	41.7km	112.5s	41.7km	675s
ne120pg2	27.8km	75s	41.7km	450s
ne120pg3	27.8km	75s	27.8km	450s

615 support (see Appendix B:). The impact of only using low-order mapping or only using
 616 *ne20* viscosity in a *ne30pg2* simulation results in a forcing spectra that lies in between
 617 the default *ne30pg2* and *ne20pg3* runs (not shown). The combined effect of both fac-
 618 tors on the forcing scale is illustrated through an *ne30pg2* simulation that uses low-order
 619 mapping, and with hyper-viscosity coefficients set to *ne20* values (*ne30pg2 – ne20visc –*
 620 *loworder* in Figure 10). The PDF of $\omega^{(gll)}$ and the forcing spectrum more closely resem-
 621 ble the *ne20pg3* run. In the *ne30pg2-ne20visc-loworder* configuration, the forcing scale
 622 is more accurately determined by Δx_{phys} since the scaled PDF is in fairly good agreement
 623 with the *ne30pg3* simulation (Figure 10c).

624 3.3.2 High Resolution

625 The experiment described in the previous section is repeated here for a *ne120pg2*
 626 aqua-planet simulation, corresponding to an approximate grid spacing of $\Delta x_{dyn} = 27.8\text{km}$
 627 and $\Delta x_{phys} = 41.7\text{km}$. *ne80pg3* refers to the grid in which the physics and dynamics
 628 are the same resolution as the physics of the *ne120pg2* grid, and *ne120pg3*, the grid in
 629 which the physics and dynamics are equal to the resolution of the dynamics of *ne120pg2*.
 630 At these higher resolutions, the solutions are sensitive to Δt_{phys} (Figure A.2), and so the
 631 *ne80* grid uses a larger time-step than that of the *ne120* grids (Table 2), following equa-
 632 tion (28).

637 Figure 11 is the same as Figure 10, but for the high resolution simulations. While
 638 the *ne80pg3* forcing spectra begins to drop off near wavenumber 100, the *ne120pg2* and
 639 *ne120pg3* drop off closer to wavenumber 200, and their spectra lie on top of one another
 640 (Figure 11a). The PDF's of (upward) $\omega^{(gll)}$ show that the *ne120* distributions lie on top
 641 of one another, and while not a perfect match, both *ne120* runs have substantially more



635 **Figure 11.** As in Figure 10, but for the high resolution simulations. Asterisks indicate that $\Delta t_{phys} = 675s$,
636 which is larger than that used for the default *ne120* runs (see Table 2).

642 frequent large magnitude vertical motion than in the *ne80pg3* run (Figure 11b). As in
643 the low resolution runs, the similarity of the *ne120* forcing spectra and $\omega^{(gll)}$ distribu-
644 tions indicate that the forcing scale of the *ne120pg2* run is not determined by the physics
645 grid spacing, but rather the dynamics grid spacing. This is also evident from the over-
646 prediction of the frequency of large magnitude $\omega^{(gll)}$ compared with the *ne120pg3* run,
647 through scaling the *ne120pg2* PDF and setting the forcing scale proportional to Δx_{phys} in
648 equation (32) (Figure 11c).

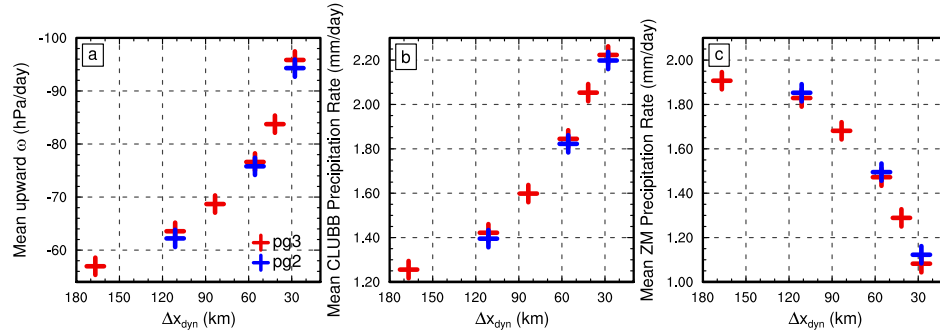
649 In the *ne120pg2* simulation, the dynamics grid determines the forcing scale for
650 the same two reasons found in the low resolution runs. The high-order mapping of the
651 physics to the dynamics is important for reconstructing scales not supported on the *pg2*
652 grid, and scaling the viscosity coefficients by the dynamics grid spacing is also important.
653 But in order to recreate the *ne80pg3* solution using the *ne120pg2* grid, the physics time-
654 steps must be the same for these two grids. Combining all three modifications leads to an
655 *ne120pg2* solution that resembles the *ne80pg3* run (*ne120pg2 – ne80visc – loworder** in
656 Figure 11). The forcing spectrum and distribution of $\omega^{(gll)}$ match that of the *ne80pg3* run,
657 and scaling the PDF by Δx_{phys} closely resembles the *ne120pg3* distribution.

658 3.3.3 Across Resolutions

659 Three intermediate resolution aqua-planets are run to provide a continuous represen-
660 tation of the solution spanning from low to high resolution (Table 3). Figure 12 is scat-
661 ter plot of the climatological global mean state versus Δx_{dyn} for all model configura-
662 tions listed in Tables 1–3. The fields plotted in the figure, upward ω , and the two components

673 **Table 3.** Δx and Δt for the physics and dynamics in the high resolution simulations. Δx is computed as the
 674 average equatorial grid spacing.

Grid name	Δx_{dyn}	Δt_{dyn}	Δx_{phys}	Δt_{phys}
ne40pg3	83.4km	222.5s	83.4km	1350s
ne60pg2	55.6km	150s	83.4km	900s
ne60pg3	55.6km	150s	55.6km	900s



675 **Figure 12.** Global mean, time-mean (a) upward ω , (b) CLUBB precipitation rate and (c) parameterized
 676 deep convective precipitation rate. All means computed from the final 11 months of one-year simulations, and
 677 upward ω is computed using 6-hourly output.

663 of precipitation, stratiform precipitation rate (CLUBB) and deep convective precipitation
 664 rate (ZM), are all sensitive to resolution. Upward ω and CLUBB precipitation decreases,
 665 and ZM precipitation increases monotonically with Δx_{dyn} . The pg2 solutions have very
 666 similar values to the pg3 solutions, although they are slightly offset towards the lower res-
 667 olution side of the plots. The differences between the pg2 and pg3 solutions are much
 668 less than the differences between pg2 and configurations where the physics and dynam-
 669 ics grids are both equal to the pg2 physics grid resolution (e.g., ne40pg3 compared with
 670 ne60pg2). The mean state of the configurations resembles that of the transients discussed
 671 in the previous sections; the coarser pg2 physics grid does not appear to degrade the re-
 672 solved scales of motion, which are primarily determined by the dynamics grid resolution.

678 4 Conclusions

679 This study documents the implementation of a coarser resolution physics grid into
 680 the Community Atmosphere Model (CAM), with spectral element dynamics (based on

a dry-mass vertical coordinate) and conservative semi-Lagrangian advection of tracers (CAM-SE-CSLAM). The spectral-element and tracer advection grids are mapped to a finite-volume physics grid after *Herrington et al.* [2018], but containing $\frac{2}{3}$ fewer degrees of freedom in each horizontal direction. Mapping from the coarser physics grid to the dynamics and tracer grids is performed with high-order reconstructions, and a tendency mapping algorithm is developed to ensure shape preservation, consistency, linear-correlation preservation and mass conservation. These numerical properties are verified to a high degree of precision through idealized tests.

The coarser resolution physics grid is designed to eliminate grid imprinting that manifests for non-smooth problems using element-based high-order Galerkin methods. The physics grid control volumes encompass a region of the element such that an isotropic representation of the numerics is provided to the physical parameterizations, and it was hypothesized that this method eliminates grid imprinting from the element boundaries. Using a Held-Suarez configuration modified with real-world topography, it was shown that element boundary noise over steep topography is eliminated from the coarser physics grid solution, consistent with our hypothesis.

Physical parameterizations make up a significant fraction of the total computational cost of atmosphere models, and the coarser physics grid may be used to reduce this overhead. The cost savings is due to the factor $\frac{4}{9}$ fewer grid columns in which the physics need be computed, and for CESM2.1, where CAM6 physics makes up about half the cost of the overall model [*Lauritzen et al.*, 2018], corresponds to a potential 25% fewer core hours. The authors sought to understand whether the reduction in computational cost occurs at the expense of a degraded solution, through aliasing the dynamics to the coarser resolution physics. An exhaustive number of grids were developed and run in an aqua-planet configuration, and confirm that the resolved scales of motion are not degraded through the use of a coarser resolution physics grid. It was found that the resolved scales are primarily determined by the effective resolution of the dynamical core. This was attributed to two factors; (1), explicit numerical dissipation by the dynamics blurs the distinction between solutions on the physics, dynamics or tracer grids, and (2), that high-order mapping of the physics tendencies to the dynamics and tracer grids reconstructs scales that are not supported on the coarser physics grid.

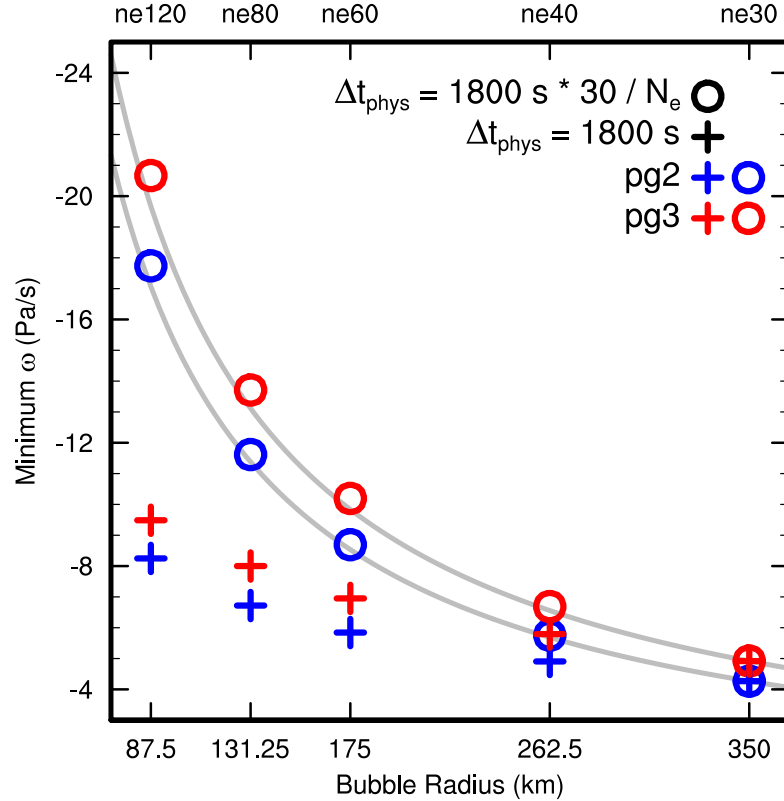
The coarser physics grid in CAM-SE-CSLAM provides significant cost savings with little to no downside. The coarser physics grid replicates solutions from the conventional method of evaluating the physics at the same resolution as the dynamical core, removes grid imprinting from the solution and runs efficiently on massively parallel systems. The coarser physics grid may be leveraged to reduce the computational burden as a component of increasingly expensive Earth System Models, or permit once unattainable throughputs for high-resolution climate simulations. The coarser physics grid configuration of CAM-SE-CSLAM is well positioned to address the scientific challenges ahead, as a formidable next generation climate model.

A: Defining Δt_{phys} across resolutions

Herrington and Reed [2018] developed a moist bubble test, which indicate that time-truncation errors are large at high resolution (about 50km or less) using more conventional values for the physics time-step. The test may be able to provide insight on a reasonable scaling of Δt_{phys} across resolutions in more complex configurations. In the test a set of non-rotating simulations are initialized with a warm, super-saturated moist bubble, and the grid spacing and bubble radius are simultaneously reduced by the same factor in each run through varying the planetary radius. The test was designed to mimic the reduction in buoyancy length scales that occur when the model resolution is increased in more complex configurations [*Hack et al.*, 2006; *Herrington and Reed*, 2018].

The moist bubble test is performed with CAM-SE-CSLAM and coupled to the simple condensation routine of *Kessler* [1969] across five different resolutions (pertaining to the *ne30*, *ne40*, *ne60*, *ne80*, and *ne120* grids). The results are expressed as the minimum ω throughout each one day simulation, and shown in Figure A.1. Two sets of simulations are performed with both *pg3* and *pg2*, one with Δt_{phys} determined by equation (28), and an equivalent set of simulations with $\Delta t_{phys} = 1800s$ for all resolutions.

With the diameters of the bubbles set proportional to Δx_{dyn} , *Herrington and Reed* [2018] has shown that ω converges to the scaling of equation (31) in the limit of small Δt_{phys} , where small Δt_{phys} refers to the CFL limiting time-step used by the dynamics. Equation (31) is overlaid as grey lines in Figure A.1, with *ne30* being the reference resolution. The solutions using Δt_{phys} from equation (28) follow the scaling, whereas fixing $\Delta t_{phys} = 1800s$ across resolutions damps the solution relative to the analytical solution,

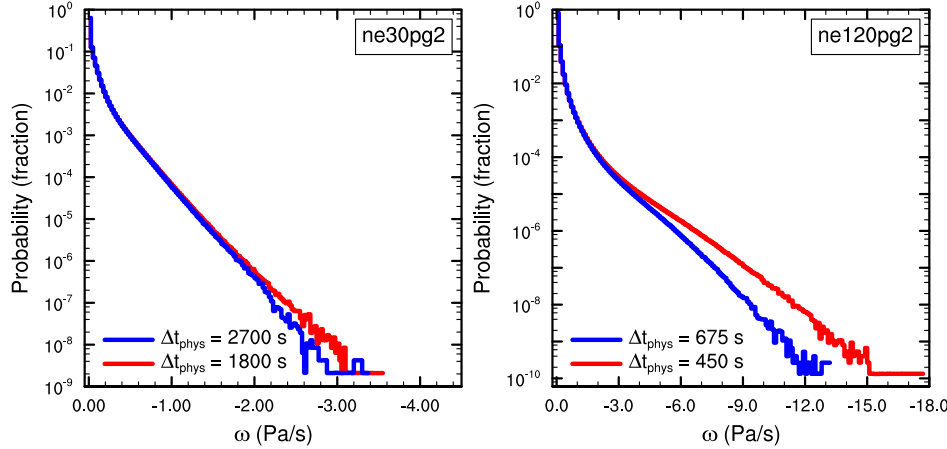


737 **Figure A.1.** The magnitude of ω in the $pg3$ solutions are systematically larger than the $pg2$ solutions,
 738 which is primarily a result of the damping effect of integrating the basis functions over a larger control vol-
 739 ume.

746 progressively more so at higher resolutions. If Δt_{phys} is too large, the solution has non-
 747 negligible error, which is avoided through scaling Δt_{phys} according to equation (28).

748 To get a handle on whether the test is useful for understanding more realistic con-
 749 figurations, four aqua-planet simulations are performed using the CAM6 physics package.
 750 A pair of $ne30pg2$ simulations, one in which Δt_{phys} is set to the appropriate value from
 751 equation (28) ($1800s$), and another where it is set to the Δt_{phys} corresponding to the $ne20$
 752 resolution ($2700s$). Similarly, a pair of $ne120pg2$ simulations are performed, one with
 753 Δt_{phys} set to the value from equation (28) ($450s$), and one with Δt_{phys} set to the $ne40$
 754 value ($675s$).

758 Figure A.2 shows the PDFs of upward ω computed from a year of six-hourly data
 759 in the simulations. At lower resolution, Δt_{phys} has only a very small effect on the solu-
 760 tion, near the tail-end of the distributions. At high-resolution, values of ω less than about



755 **Figure A.2.** Probability density distribution of upward ω everywhere in the model in the aqua-planets using
 756 the *ne30pg2* grid (Left) and the *ne120pg2* grid (Right). Figure computed for one year of 6-hourly data. The
 757 different colors indicate the physics time-steps used in the runs.

761 -3Pa/s are more frequent in the small Δt_{phys} run, with the discrepancy growing more for
 762 larger magnitudes of ω . The progressively larger errors with increasing resolution also
 763 manifests in the moist bubble tests, indicating that truncation errors arising from large
 764 Δt_{phys} do exist in more complex configurations.

765 **B: The impact of high-order mapping to the dynamics grids**

766 Figure B.1a shows a close-up of the wavenumber power spectrum of the forcing on
 767 the *pg* grid (dotted), where it is computed, and on the *GLL* grid (solid), where it is has
 768 been mapped. In *ne30pg3*, the magnitudes are similar on both grids, except the mapping
 769 tends to damp the high wavenumbers of the forcing on the *GLL* grid (greater than 60),
 770 but these scales are primarily below the effective resolution of the model and should not
 771 effect the solution. For *ne30pg2*, the magnitude of the forcing is actually greater after
 772 mapping to the *GLL* grid, and more similar to the forcing in the *ne30pg3* simulations.
 773 The high-order mapping can therefore replicate the scales of the physics tendencies that
 774 occur in the *pg3* simulation, even though the physics are evaluated on a coarser *pg2* grid.

779 The importance of the high-order mapping can be shown with an additional *ne30pg2*
 780 simulation, using low-order mapping (*ne30pg2 – loworder* in Figure B.1). Specifically,
 781 low-order mapping refers to piecewise constant mapping between the *pg2* and *CSLM*

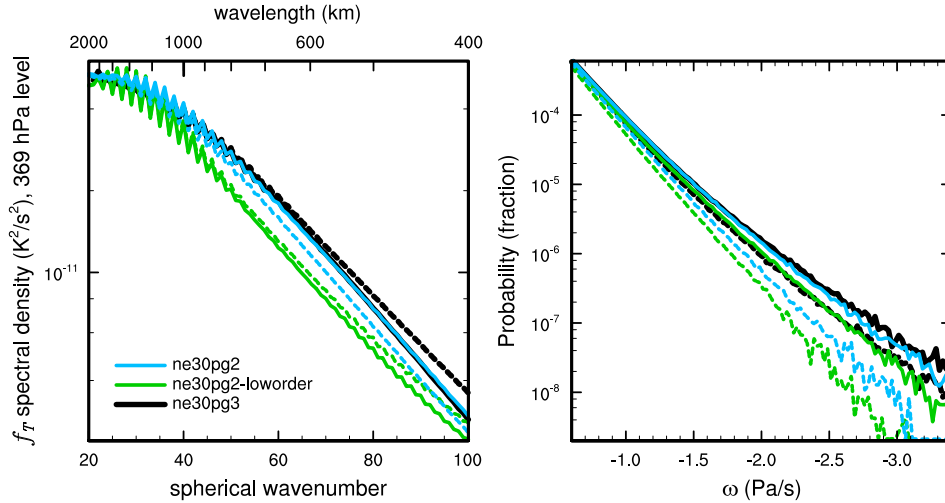


Figure B.1. (Left) Wavenumber-power spectrum of the temperature tendencies from the moist physics, at the 369 hPa level, and (right) probability density distribution of upward ω , everywhere in the model, for three year-long aqua-planet simulations. Solid lines refer to values of on the *GLL* grids, and dashed lines, the fields on the *pg* grids. See text for details regarding the three simulations.

grids, and bi-linear mapping from *pg2* to the *GLL* grid. The forcing spectrum is now similar on both the *pg2* and *GLL* grids, although the low-order mapping tends to damp the forcing on the *GLL* grid for wavenumbers greater than about 60, scales smaller than the models effective resolution (Figure B.1a). A close up of the PDF of $\omega^{(gll)}$ is provided in Figure B.1b (solid lines). As expected, the frequency of large magnitude $\omega^{(gll)}$ in the low-order run is less compared to the default *ne30pg2* simulation.

The dotted lines in Figure B.1b show the PDF of ω on the *pg* grids. The frequency of large magnitude ω is reduced on the *pg* grids, compared to the state on the *GLL* grids. This is primarily due to the smoothing effect of integrating the nodal point values over control volumes (H18). The larger ω values are even less frequent on the *pg2* grid due to integrating over control volumes $\frac{9}{4}$ times greater than the *pg3* control volumes.

Acknowledgments

The National Center for Atmospheric Research (NCAR) is sponsored by the National Science Foundation. We thank NCAR's Computational and Information Systems Lab (CISL) for providing computing support. Herrington, Reed, and Lauritzen are indebted to the NCAR Advanced Study Program graduate visitor program for funding Herring-

ton's 12-month visit. Reed was partially supported by U.S. Department of Energy Office of Science grant DE-SC0019459. Goldhaber was partially supported by the U.S. Department of Energy Office of Biological and Environmental Research, Work Package 12-015334 "Multiscale Methods for Accurate, Efficient, and Scale-Aware Models of the Earth System". Model output used in this study is publicly available from <https://github.com/adamrher/2017-physics/tree/master/data>.

804 References

- 805 Barth, T., and D. Jespersen (1989), The design and application of upwind schemes on un-
 806 structured meshes., *Proc. AIAA 27th Aerospace Sciences Meeting, Reno.*
- 807 Brdar, S., M. Baldauf, A. Dedner, and R. Klöfkorn (2013), Comparison of dynamical
 808 cores for nwp models: comparison of cosmo and dune, *Theoretical and Computational*
 809 *Fluid Dynamics*, 27(3-4), 453–472, doi:10.1007/s00162-012-0264-z.
- 810 Computational and Information Systems Laboratory (2017), Cheyenne: HPE/SGI ICE XA
 811 System (AMP Model Developments), doi:10.5065/D6RX99HX.
- 812 Dennis, J. M., J. Edwards, K. J. Evans, O. Guba, P. H. Lauritzen, A. A. Mirin, A. St-Cyr,
 813 M. A. Taylor, and P. H. Worley (2012), CAM-SE: A scalable spectral element dynami-
 814 cal core for the Community Atmosphere Model, *Int. J. High. Perform. C.*, 26(1), 74–89,
 815 doi:10.1177/1094342011428142.
- 816 Giraldo, F., and M. Restelli (2008), A study of spectral element and discontinuous
 817 galerkin methods for the Navier-Stokes equations in nonhydrostatic mesoscale atmo-
 818 spheric modeling: Equation sets and test cases, *J. Comput. Phys.*, 227(8), 3849 – 3877,
 819 doi:<http://dx.doi.org/10.1016/j.jcp.2007.12.009>.
- 820 Hack, J., M. Caron, G. Danabasoglu, K. W. Oleson, C. Bitz, and J. Truesdale (2006),
 821 CCSM–cam3 climate simulation sensitivity to changes in horizontal resolution, *J. Cli-
 822 mate*, 19(1), 2269–2289, doi:10.1175/JCLI3764.1.
- 823 Held, I. M., and M. J. Suarez (1994), A proposal for the intercomparison of the dynamical
 824 cores of atmospheric general circulation models, *Bull. Am. Meteorol. Soc.*, 73, 1825–
 825 1830.
- 826 Herrington, A., and K. Reed (2018), An idealized test of the response of the commu-
 827 nity atmosphere model to near-grid-scale forcing across hydrostatic resolutions, *J. Adv.*
 828 *Model. Earth Syst.*, 10(2), 560–575.

- 829 Herrington, A., P. Lauritzen, M. A. Taylor, S. Goldhaber, B. E. Eaton, J. Bacmeister,
830 K. Reed, and P. Ullrich (2018), Physics-dynamics coupling with element-based high-
831 order galerkin methods: quasi equal-area physics grid, *Mon. Wea. Rev.*, 47, 69–84, doi:
832 10.1175/MWR-D-18-0136.1.
- 833 Herrington, A. R., and K. A. Reed (2017), An explanation for the sensitivity of the mean
834 state of the community atmosphere model to horizontal resolution on aquaplanets, *J.
835 Climate*, 30(13), 4781–4797, doi:10.1175/jcli-d-16-0069.1.
- 836 Jablonowski, C., and D. L. Williamson (2011), The pros and cons of diffusion, filters and
837 fixers in atmospheric general circulation models., in: P.H. Lauritzen, R.D. Nair, C.
838 Jablonowski, M. Taylor (Eds.), Numerical techniques for global atmospheric models,
839 *Lecture Notes in Computational Science and Engineering*, Springer, 80.
- 840 Jeevanjee, N. (2017), Vertical velocity in the gray zone, *Journal of Advances in Modeling
841 Earth Systems*, 9(6), 2304–2316, doi:10.1002/2017MS001059.
- 842 Jeevanjee, N., and D. M. Romps (2016), Effective buoyancy at the surface and aloft,
843 *Quart. J. Roy. Meteor. Soc.*, 142(695), 811–820.
- 844 Jöckel, P., R. von Kuhlmann, M. G. Lawrence, B. Steil, C. Brenninkmeijer, P. J. Crutzen,
845 P. J. Rasch, and B. Eaton (2001), On a fundamental problem in implementing flux-form
846 advection schemes for tracer transport in 3-dimensional general circulation and chem-
847 istry transport models., *Q.J.R. Meteorol. Soc.*, 127(573), 1035–1052.
- 848 Jones, P. W. (1999), First- and second-order conservative remapping schemes for grids in
849 spherical coordinates, *Mon. Wea. Rev.*, 127, 2204–2210.
- 850 Kessler, E. (1969), On the distribution and continuity of water substance in atmospheric
851 circulations, *Meteorol. Monogr.*, 10(32), 88.
- 852 Lander, J., and B. Hoskins (1997), Believable scales and parameterizations in a spectral
853 transform model, *Mon. Wea. Rev.*, 125, 292–303., doi:10.1175/1520-0493.
- 854 Lauritzen, P., and J. Thuburn (2012), Evaluating advection/transport schemes using inter-
855 related tracers, scatter plots and numerical mixing diagnostics, *Quart. J. Roy. Met. Soc.*,
856 138(665), 906–918, doi:10.1002/qj.986.
- 857 Lauritzen, P. H., and D. L. Williamson (2019), A total energy error analysis of dynamical
858 cores and physics-dynamics coupling in the community atmosphere model (cam), *J.
859 Adv. Model. Earth Syst.*, doi:10.1029/2018MS001549.
- 860 Lauritzen, P. H., R. D. Nair, and P. A. Ullrich (2010), A conservative semi-Lagrangian
861 multi-tracer transport scheme (CSLAM) on the cubed-sphere grid, *J. Comput. Phys.*,

- 862 229, 1401–1424, doi:10.1016/j.jcp.2009.10.036.
- 863 Lauritzen, P. H., P. A. Ullrich, and R. D. Nair (2011), Atmospheric transport schemes:
864 desirable properties and a semi-Lagrangian view on finite-volume discretizations, in:
865 P.H. Lauritzen, R.D. Nair, C. Jablonowski, M. Taylor (Eds.), Numerical techniques for
866 global atmospheric models, *Lecture Notes in Computational Science and Engineering*,
867 Springer, 2011, 80, doi:10.1007/978-3-642-11640-7_8.
- 868 Lauritzen, P. H., W. C. Skamarock, M. J. Prather, and M. A. Taylor (2012), A standard
869 test case suite for 2d linear transport on the sphere, *Geo. Geosci. Model Dev.*, 5, 887–
870 901.
- 871 Lauritzen, P. H., A. J. Conley, J.-F. Lamarque, F. Vitt, and M. A. Taylor (2015a), The ter-
872 minator "toy" chemistry test: a simple tool to assess errors in transport schemes, *Geo-*
873 *scientific Model Development*, 8(5), 1299–1313, doi:10.5194/gmd-8-1299-2015.
- 874 Lauritzen, P. H., J. T. Bacmeister, P. F. Callaghan, and M. A. Taylor (2015b), Ncar global
875 model topography generation software for unstructured grids, *Geoscientific Model Devel-*
876 *opment Discussions*, 8(6), 4623–4651, doi:10.5194/gmdd-8-4623-2015.
- 877 Lauritzen, P. H., M. A. Taylor, J. Overfelt, P. A. Ullrich, R. D. Nair, S. Goldhaber, and
878 R. Kelly (2017), CAM-SE-CSLAM: Consistent coupling of a conservative semi-
879 lagrangian finite-volume method with spectral element dynamics, *Mon. Wea. Rev.*,
880 145(3), 833–855, doi:10.1175/MWR-D-16-0258.1.
- 881 Lauritzen, P. H., R. Nair, A. Herrington, P. Callaghan, S. Goldhaber, J. Dennis, J. T.
882 Bacmeister, B. Eaton, C. Zarzycki, M. A. Taylor, A. Gettelman, R. Neale, B. Dob-
883 bins, K. Reed, and T. Dubos (2018), NCAR CESM2.0 release of CAM-SE: A refor-
884 mulation of the spectral-element dynamical core in dry-mass vertical coordinates with
885 comprehensive treatment of condensates and energy, *J. Adv. Model. Earth Syst.*, doi:
886 10.1029/2017MS001257.
- 887 Medeiros, B., D. L. Williamson, and J. G. Olson (2016), Reference aquaplanet climate in
888 the community atmosphere model, version 5, *J. Adv. Model. Earth Syst.*, 8(1), 406–424,
889 doi:10.1002/2015MS000593.
- 890 Nair, R., H.-W. Choi, and H. Tufo (2009), Computational aspects of a scalable high-order
891 discontinuous galerkin atmospheric dynamical core, *Computers & Fluids*, 38(2), 309 –
892 319, doi:<http://dx.doi.org/10.1016/j.compfluid.2008.04.006>.
- 893 Nair, R. D., and P. H. Lauritzen (2010), A class of deformational flow test cases for linear
894 transport problems on the sphere, *J. Comput. Phys.*, 229, 8868–8887, doi:10.1016/j.jcp.

- 895 2010.08.014.
- 896 Neale, R. B., and B. J. Hoskins (2000), A standard test for agcms including their physical
897 parametrizations: I: the proposal, *Atmos. Sci. Lett.*, 1(2), 101–107, doi:10.1006/asle.2000.
898 0022.
- 899 Neale, R. B., C.-C. Chen, A. Gettelman, P. H. Lauritzen, S. Park, D. L. Williamson, A. J.
900 Conley, R. Garcia, D. Kinnison, J.-F. Lamarque, D. Marsh, M. Mills, A. K. Smith,
901 S. Tilmes, F. Vitt, P. Cameron-Smith, W. D. Collins, M. J. Iacono, R. C. Easter, S. J.
902 Ghan, X. Liu, P. J. Rasch, and M. A. Taylor (2012), Description of the NCAR Commu-
903 nity Atmosphere Model (CAM 5.0), *NCAR Technical Note NCAR/TN-486+STR*, National
904 Center of Atmospheric Research.
- 905 Pauluis, O., and S. Garner (2006), Sensitivity of radiative–convective equilibrium simula-
906 tions to horizontal resolution, *J. Atmos. Sci.*, 63(7), 1910–1923.
- 907 Randall, D., M. Khairoutdinov, A. Arakawa, and W. Grabowski (2003), Breaking the
908 cloud parameterization deadlock, *Bulletin of the American Meteorological Society*,
909 84(11), 1547–1564.
- 910 Shutts, G. (2005), A kinetic energy backscatter algorithm for use in ensemble prediction
911 systems, *Quart. J. Roy. Meteorol. Soc.*, 131, 3079–3102.
- 912 Skamarock, W. (2011), Kinetic energy spectra and model filters, in: P.H. Lauritzen, R.D.
913 Nair, C. Jablonowski, M. Taylor (Eds.), Numerical techniques for global atmospheric
914 models, *Lecture Notes in Computational Science and Engineering*, Springer, 80.
- 915 Taylor, M., J. Edwards, and A. St-Cyr (2008), Petascale atmospheric models for the com-
916 munity climate system model: new developments and evaluation of scalable dynamical
917 cores, *J. Phys.: Conf. Ser.*, 125, doi:10.1088/1742-6596/125/1/012023.
- 918 Wan, H., P. J. Rasch, M. A. Taylor, and C. Jablonowski (2015), Short-term time step con-
919 vergence in a climate model, *Journal of advances in modeling earth systems*, 7(1), 215–
920 225, doi:10.1002/2014MS000368.
- 921 Wedi, N. P. (2014), Increasing horizontal resolution in numerical weather prediction and
922 climate simulations: illusion or panacea?, *Philosophical Transactions of the Royal So-
923 ciety of London A: Mathematical, Physical and Engineering Sciences*, 372(2018), doi:
924 10.1098/rsta.2013.0289.
- 925 Weisman, M. L., W. C. Skamarock, and J. B. Klemp (1997), The resolution dependence
926 of explicitly modeled convective systems, *Monthly Weather Review*, 125(4), 527–548,
927 doi:10.1175/1520-0493(1997)125<0527:TRDOEM>2.0.CO;2.

- 928 Williamson, D. L. (1999), Convergence of atmospheric simulations with increasing
929 horizontal resolution and fixed forcing scales, *Tellus A*, 51, 663–673, doi:10.1034/j.
930 1600-0870.1999.00009.x.
- 931 Williamson, D. L. (2013), The effect of time steps and time-scales on parametrization
932 suites, *Quart. J. Roy. Meteor. Soc.*, 139(671), 548–560, doi:10.1002/qj.1992.
- 933 Williamson, D. L., and J. G. Olson (2003), Dependence of aqua-planet simulations on
934 time step, *Q. J. R. Meteorol. Soc.*, 129(591), 2049–2064.
- 935 Zhang, G., and N. McFarlane (1995), Sensitivity of climate simulations to the parameter-
936 ization of cumulus convection in the canadian climate center general-circulation model,
937 *ATMOSPHERE-OCEAN*, 33(3), 407–446.